Understanding the emergence of the boson peak in molecular glasses

Mario González-Jiménez,[1] Trent Barnard,[2] Ben A. Russell,[1] Nikita V. Tukachev,[1] Uroš Javornik,[3] Laure-Anne Hayes,[1] Andrew J. Farrell,[1] Sarah Guinane,[1] Hans M. Senn,[1] Andrew J. Smith,[4] Martin Wilding,[5] Gregor Mali,[3] Motohiro Nakano,[6] Yuji Miyazaki,[6] Paul McMillan,[7] Gabriele C. Sosso,[2*] Klaas Wynne[1*]

[1]School of Chemistry, University of Glasgow, UK
[2]Department of Chemistry, University of Warwick, UK
[3]Department of Inorganic Chemistry and Technology, National Institute of Chemistry, Ljubljana, Slovenia
[4]Diamond Light Source, Harwell Science and Innovation Campus, UK
[5]School of Chemistry, University of Cardiff, UK
[6]Research Center for Thermal and Entropic Science, Osaka University, Japan
[7]Dept. of Chemistry, University College London, UK

One of the common features of a glass is the so-called "boson peak", observed as an excess in the heat capacity over the crystal or as an additional peak in the terahertz vibrational spectrum. The microscopic origins of the boson peak are controversial, albeit the emergence of locally ordered structures inhibiting crystallisation has been put forward as a possible culprit. Unfortunately, the terahertz spectral range is often congested with many other contributions complicating observation of the boson feature. Here, we show that depolarised Raman scattering—obtained using femtosecond optical Kerr-effect spectroscopy in liquids consisting of highly symmetric molecules—can be used to isolate the boson peak, allowing its detailed observation over a wide range of temperatures from the (supercooled) liquid into the glass. The boson peak in the vibrational spectrum matches the excess heat capacity observed in low-temperature heat capacity measurements. As the boson peak intensifies on cooling towards the glass transition, wide-angle x-ray scattering shows the simultaneous appearance of a pre-peak due to molecular clusters consisting of *circa* 20 molecules. Atomistic molecular dynamics simulations—reproducing both boson and pre peaks—indicate that these clusters are caused by over-coordinated molecules tending towards but prevented from attaining crystalline structural order. These findings represent an essential step toward our understanding of the physics of vitrification.

Glasses are prepared by the rapid cooling of liquids (while avoiding crystal nucleation) and are therefore solids with some of the disorder of the liquid phase frozen in. When a liquid is (super) cooled, the primary or α relaxation rate—directly related to viscous flow—decreases and drops towards zero somewhere near the glass-transition temperature T_g, where calorimetry measurements identify a rapid decrease in heat capacity.[1] Below the glass-transition, secondary or β-relaxation processes occur due to faster dynamic processes that become uncoupled from the α-relaxation on vitrification and are the dominant relaxation channel in the glassy state.[2]

The molecular origin of these secondary relaxations is still unclear.[3] Because secondary relaxations were first observed in polymer glasses, they were assumed to originate in the small angle orientational diffusion of the side chains or functional groups of the polymers and therefore of essentially intramolecular character. However, the observation of secondary relaxations in rigid polymer glasses and even metallic glasses[2] implies that at least some (now referred to as "Johari-Goldstein") secondary relaxations are of an intermolecular character. One suggestion is that they are caused by spatial inhomogeneities[4] giving rise to more loosely packed regions, distinct relaxing domains, defects,[5,6] or regions of different packing such as locally favoured *vs*. liquid-like structures.[7] Another approach starts from the liquid's potential energy landscape and views secondary relaxations as transitions between neighbouring potential energy minima while primary relaxation corresponds to the higher energy transitions between mega basins.[1] This picture explains why α relaxation is frozen out before β relaxations.

Another phenomenon often associated with the glass is the **boson peak**,[1] which is observed as an excess intensity of low frequency modes around about 1 THz in spectroscopic studies or as an excess heat capacity signature. The origin of the phenomenon has been assigned various interpretations, ranging from the occurrence of "two-level" excitations associated with broken bond or other defects in glasses,[8] to other mechanisms for creating an excess in the low frequency vibrational density of states in the terahertz range over that expected for dispersive phonons in a perfect crystal, giving rise to an additional contribution to the very low temperature heat

capacity C_p leading to a peak in C_p/T^3.[9] The presence of the boson peak has been linked to fluctuating elastic constants within a structurally disordered amorphous matrix,[10] quasi-localised soft potential defects,[11,12] localisation of transverse phonons associated with defective soft structures,[13] (quasi-)localised vibrational modes of locally favoured structures,[14] a crystal-like van Hove singularity near the pseudo Brillouin zone edge washed out by structural disorder,[15] may be caused by diffusive damping rather than spatial disorder,[16] and might not even contribute any extra heat capacity.[17]

Both Johari-Goldstein β relaxations and the boson peak are intermolecular in nature. Therefore, a study of the intermolecular structure and dynamics in supercooled and vitrified liquids could provide insight into these phenomena. Intermolecular modes have been observed using various techniques including inelastic neutron, x-ray, and Raman scattering as well as infrared and dielectric relaxation spectroscopy. However, in these techniques the intermolecular modes are typically (partially) obscured by other terahertz frequency bands, such as low-frequency vibrations, librations, and (above the glass transition) orientational and translational relaxation bands. This complicates lineshape analysis.

We have shown that symmetry can be used to simplify the depolarised Raman spectra of liquids in the terahertz range.[18–20] The orientational-relaxation and librational bands are proportional to the anisotropic part of the molecular polarisability tensor, which vanishes for molecules with tetrahedral or octahedral symmetry, leaving a simplified spectrum. The disadvantage of Raman spectroscopy is that the Raman coupling coefficient has a frequency dependence that is unknown in principle[21] although it is experimentally found to be linearly proportional to frequency.[22–25] Inelastic neutron and x-ray scattering, on the other hand, are sensitive to the movements of all atoms and have no frequency-dependent coupling coefficient. However, the clear advantage of Raman spectroscopy is selectivity through symmetry and (in the technique used here) greater signal to noise over a wide frequency range. Thus, it would be enormously advantageous to study liquids of symmetric molecules that also readily vitrify into a glass. However, in practice this appears to be a contradiction in terms.

The alkoxides of early transition metals such as Ti and Zr and group 14 elements (Si, Ge, *etc*.) are important compounds in their liquid state, providing precursors for sol-gel and chemical vapour deposition technologies for the production of sols, gels and ceramics, including zeolites,[26] periodic mesoporous silicas,[27] organosilicas,[28] and materials with photocatalytic and superhydrophobic properties.[29,30] The transition metal alkoxides ($M(OR)_n$) oligomerise while exhibiting rapid ligand exchange due to the labile nature of the M-O bonds and the ability of the metal centres to adopt a coordination higher than four.[31] In contrast, silicon-based alkoxides such as $Si(OBu)_4$ (tetrabutyl orthosilicate) do not exhibit ligand lability and do not normally oligomerise. All of these liquids are known to hydrolyse readily to form amorphous metal-oxide gels and organic–inorganic hybrid materials.[32]

Here we show that tetrabutyl orthosilicate (TBOS) is an example of a class of monomeric tetrahedrally symmetric molecular liquids that nonetheless vitrify. In fact, it was impossible to make these compounds crystallise at all. TBOS was studied with sub-terahertz depolarised Raman spectroscopy, synchrotron x-ray scattering, calorimetry, and atomistic molecular dynamics simulations to gain insights into the temperature-dependent relaxation processes and their dynamic signatures in relation to structural changes that occur within the liquid and glassy states. It is found that the depolarised Raman spectra are indeed greatly simplified due to the molecular symmetry. This allowed us to separate α-relaxation processes from non-diffusive modes, in particular intermolecular modes. Detailed temperature-dependent lineshape analysis of these intermolecular modes shows that in TBOS, they are inhomogeneously broadened and split into two clearly identifiable bands developing differently with temperature. The behaviour of the lower frequency of these two bands is consistent with that of the boson peak. Analysis of the first sharp diffraction peak in temperature-dependent small and wide-angle x-ray scattering experiments show inhomogeneous broadening and a weak pre-peak in the glass—corresponding to clusters about three TBOS molecules across—consistent with the OKE results. Molecular dynamics simulations reveal an increase in the average coordination number of TBOS molecules in the glass, which manifests itself as a change in the topology of the disordered network. In particular, by means of a Voronoi analysis, we pinpoint the emergence of specific molecular environments, unique to the glass, consisting of clusters of 3-4 TBOS molecules. In addition, the topology of these Voronoi polyhedral suggests the emergence of BCC order—the extent of which remains minimal even upon cooling—and thus prevents the system from crystallising, consistent with the experimental data. These topological features might also be responsible for the emergence of the pre-peak in the x-ray scattering experiments.

Results

Tetrabutyl orthosilicate (TBOS) is a viscous liquid that does not crystallise and has a glass transition temperature T_g as measured by calorimetry (see Supplementary Figure 1) of 124 K. The experimentally determined shear viscosity of TBOS is shown in Supplementary Figure 2 together with a fit to the Vogel-Fulcher-Tammann equation with $T_0 = 105.4 \pm 0.5$ K. As $T_0 < T_g$ here, this indicates that TBOS is a fragile glass former consistent with the shape of the glass transition in calorimetry.[1]

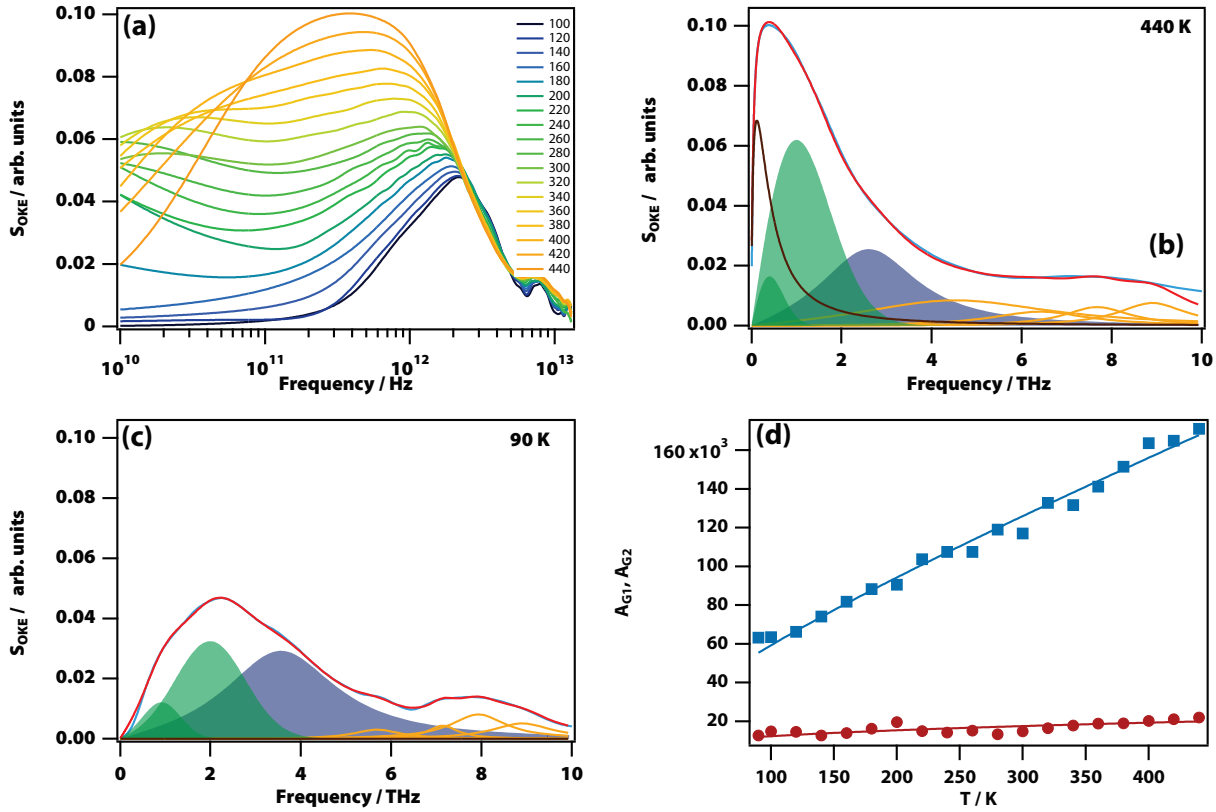

Figure 1. Optical Kerr-effect (OKE) spectra of supercooled and vitrified tetrabutyl orthosilicate (TBOS). (**a**) All data from 100 to 440 K. (**b-c**) Two representative temperatures and fits. The two green bands at low frequency are intermolecular modes fitted to two Gaussian functions; the blue band is an intramolecular vibration fitted to a Brownian oscillator function with constant amplitude. The yellow curves are additional intramolecular vibrations. (**d**) Temperature-dependent amplitudes of the low frequency (A_{G1}, red disks) and high frequency (A_{G2}, blue squares) intermolecular modes. The lines are guides to the eye. While these amplitudes change, the amplitude of the higher frequency intramolecular modes remain unchanged with temperature as expected.

Femtosecond optical Kerr-effect (OKE) spectroscopy[33,34] was used to measure the Bose-Einstein corrected depolarised Raman spectrum using a time-resolved pump-probe technique and numerical Fourier deconvolution. In our set-up,[19,20,35,36] which has a time resolution of about 20 fs, the pump-probe delay can be as large as 4 ns resulting in spectra with a maximum spectral range from 125 MHz to 50 THz but is limited here to the range 10 GHz to ~10 THz to maximise the signal to noise in the data.

The low-frequency depolarised Raman spectra of liquids typically contain (overlapping) contributions from orientational relaxation, translational relaxation, intermolecular cage rattling motions, librations, and vibrations. [37,38] We have shown that—at least within the accessible frequency range >1 GHz—the orientational and translational relaxations in nearly all liquids follow the Stokes-Einstein-Debye and Stokes-Einstein laws tracking the macroscopic shear viscosity and are therefore representative of primary or α relaxations.[20]

The amplitudes of orientational relaxation and librations in the spectra are proportional to the anisotropic molecular polarisability tensor, which vanishes in a molecule with tetrahedral, octahedral, or icosahedral symmetry. Quantum chemistry calculations were carried out on TBOS (see Methods) and stability calculations of dimers, trimers, and higher aggregates show that TBOS is expected to remain monomeric under normal conditions. The calculated infrared spectrum in the Si-O-C stretch region (around 1,100 cm^{-1}) matches the experimental one (see Supplementary Figure 3) confirming that TBOS is monomeric and the silicon atom tetrahedrally coordinated as expected. Temperature-dependent ^{13}C NMR spectroscopy from 20° to -50°C shows 4 four sharp bands as expected for a monomer (see Supplementary Figure 4).

Calculation of the molecular polarisability tensor of 100 structures randomly picked from 31,500 low-energy conformers shows that the anisotropic polarisability remains an order of magnitude smaller than the isotropic one, demonstrating that the deviation from perfect tetrahedrality due to the flexibility of the butoxy sidechains has a minimal effect. Therefore, the spectrum of TBOS should be greatly simplified due to symmetry, only showing translational relaxation, intermolecular cage rattling motions, and vibrations.

The OKE spectra. OKE spectra of TBOS were obtained over a temperature range from 90 to 440 K as shown in Figure 1 (also see Supplementary Figure 5 and Supplementary Figure 6 for individual spectra). The spectra are largely temperature independent ≥3 THz as this region only has intramolecular modes. The low frequency (≤3 THz) part of the spectra has a strong temperature dependence with changes in shape as well as amplitude.

The spectra in this low frequency range could be fitted consistently with four functions (see also Supplementary note 1 for details and Supplementary Table 1 for fit parameters): a Havriliak-Negami function representing the diffusive α relaxation, two Gaussian functions representing the intermolecular modes, and a Brownian oscillator function for the lowest frequency intramolecular mode. As expected, the diffusive relaxation is strongly temperature dependent and freezes out below the glass transition. An Arrhenius plot of the relaxation time constant is shown Supplementary Figure 7 showing that it closely follows the temperature-dependent macroscopic shear viscosity through the Stokes-Einstein law, as expected for translational relaxation, and demonstrating it is an α relaxation. The Brownian oscillator has a constant amplitude consistent with an intramolecular mode.

The amplitudes of the two Gaussians (see Figure 1) are proportional to temperature, showing that they are collision-induced intermolecular "cage rattling" modes. The spectra below the glass transition (for example at 90 K in Figure 1) clearly show the two intermolecular bands as a peak at 2 THz and a shoulder at 1 THz. As can be seen in Figure 2, the two intermolecular bands evolve differently as a function of temperature. The ratio of the amplitudes of the low and high frequency bands stays approximately constant at high temperature but doubles on cooling to the glass transition. The width of the high frequency band is essentially temperature independent suggesting the corresponding inhomogeneity is constant. The width of the low frequency band slightly increases on cooling and plateaus below ~200 K but this is a minor effect. The centre frequency of both bands increases on cooling in a linear fashion for the high frequency and a nonlinear fashion for the low frequency band, the latter plateauing below the glass transition.

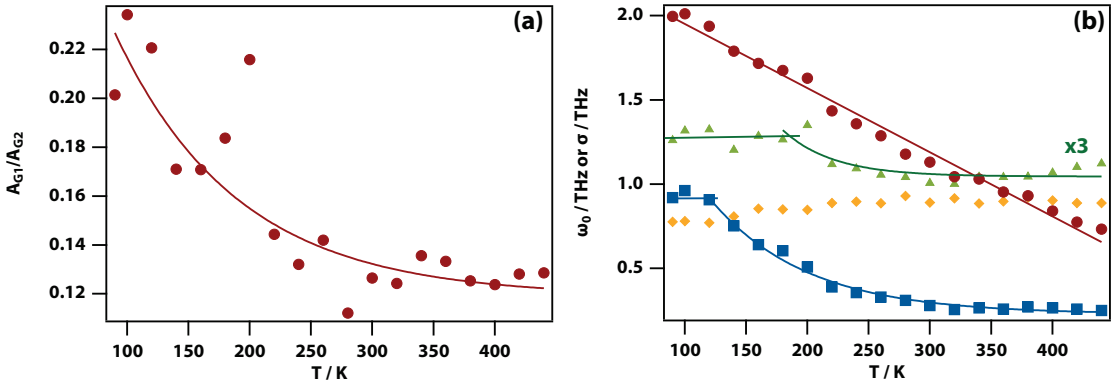

Figure 2. Temperature dependence of the fit parameters for the intermolecular modes. (**a**) Ratio of the amplitude of the low-frequency intermolecular mode over that of the high frequency one. The solid red line is an exponential fit to guide the eye (The data point at 200 K was omitted in this fit on account of the noise at low frequencies in the corresponding OKE data). (**b**) Centre frequency of the two intermolecular modes (red disks and blue squares, also shown are linear and exponential fits to guide the eye) and the corresponding widths (yellow diamonds and green triangles respectively, also shown are an exponential fit and a horizontal line to guide the eye).

WAXS and Raman experiments. Structural information can be obtained using small (SAXS) and wide-angle x-ray scattering (WAXS) experiments carried out over a similar temperature range as the OKE experiments with a 2 K step size (see Figure 3 and Supplementary Figure 8). The first sharp diffraction peak at ~0.65 $Å^{-1}$ is consistent with the Si–Si nearest neighbour distance of 10.4 Å calculated from the liquid density (see Supplementary Figure 9).

The SWAXS intensity data were analysed by curve fitting, requiring a Gaussian function to fit the first sharp diffraction peak and a Lorentzian for the second (see Supplementary note 2 and Supplementary Table 2 for the fit parameters). The fits were used to calculate the radial distribution functions using analytical transformation, showing a reduction of the first and second solvation shell radius on cooling as expected (see Supplementary Figure 10).

Figure 3(b) and (c) show the evolution of the peak position and width of the first and second sharp diffraction peak as a function of temperature. The first sharp diffraction peak shifts in a nonlinear fashion to lower q on cooling, while the second peak linearly shifts to higher q. Both show a distinct change in their evolution below 110 K, which is slightly below the glass transition temperature as determined using calorimetry (124 K). Temperature dependent Raman spectra of the CH-stretch band (Supplementary Figure 11) show that, on lowering the temperature, the TBOS molecules reduce the number of gauche defects in the alkoxide side chains, consistent with the lowering of the peak position of the first sharp diffraction peak on cooling.

Close inspection of the data at the lowest temperatures shows the presence of a weak pre-peak at $q \sim 0.2$ $Å^{-1}$, however, the signal-to-noise in the SAXS–WAXS transition region is insufficient for full temperature-dependent analysis of this feature. The 9 lowest temperature data sets ($\leq$ 110 K) were averaged for improved signal-to-noise revealing a clear pre-peak. This spectrum could be fitted with an additional Gaussian, allowing a determination of the pre-peak position as 0.234 $Å^{-1}$ (see Supplementary Table 3 for fit parameters).

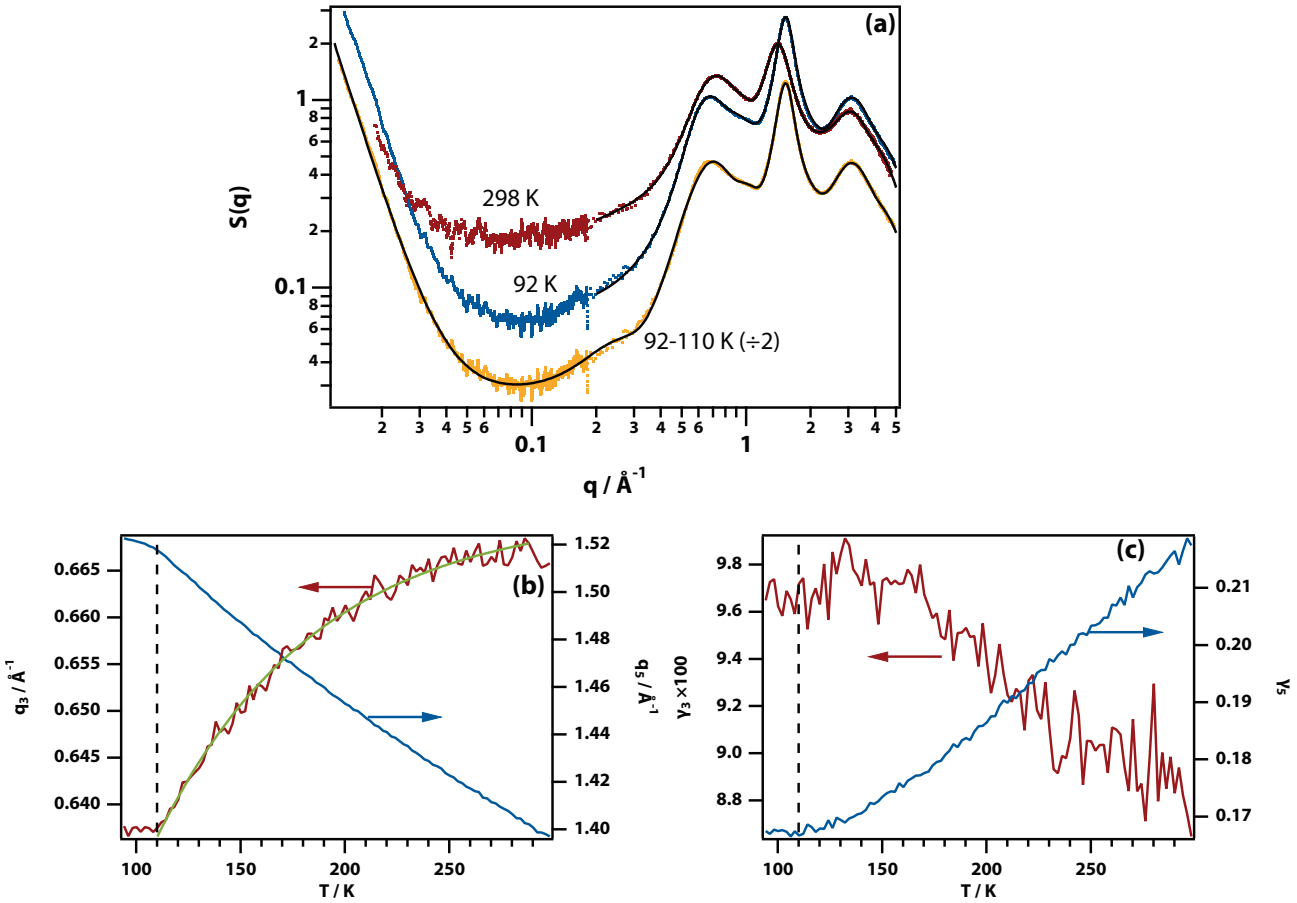

Figure 3. Analysis of temperature dependent WAXS data. (**a**) Experimental SAXS and WAXS data taken at 298 K (red) and 92 K (blue) and fit to four Gaussians and a Lorentzian (black). The average of the nine data sets at 110 K and below is shown (yellow) with a fit including an additional Gaussian to account for the pre-peak (black). (**b**) Variation of the peak of the first (red) and second (blue) sharp diffraction peaks in the WAXS data obtained from fits to a Gaussian and a Lorentzian respectively. The green line is an exponential fit to guide the eye. (**c**) Variation of the width of the first (red) and second (blue) sharp diffraction peaks.

MD simulations. Atomistic MD simulations over more than 1μs (see Methods and Supplementary note 3 for details) were used to generate a 512-molecule model of liquid TBOS quenched at a rate of 3.2×10^8 K/s into the glass. The resulting T_g is 249±20 K (see Supplementary Figure 12), significantly higher than the experimental value (124 K) due to the much faster cooling rate. The Fourier transform of the Si-Si velocity-velocity autocorrelation function (Figure 4(a)), which thanks to the molecular symmetry should be similar to the OKE spectra, indeed shows good agreement including a decrease of signal intensity and shift to higher frequencies on cooling. Computation of the total Si-Si (static) structure factor (Figure 4(b)) shows the emergence of a low-q feature on cooling at 0.25 Å^{-1} consistent with the pre-peak observed experimentally (Figure 3(a)).

The Si-Si pair correlation function (Figure 4(c)) shows a significant increase in short-range order, particularly in the second coordination shell. The first coordination shell (≤~6 Å, see Figure 4(d)) only contains about 2 molecules, showing a lack of tetrahedral order in both liquid and glassy TBOS. However, the second coordination shell (≤~12 Å) contains about 12 molecules.

A Voronoi analysis using the Si atoms was performed (Fig.5(a)) to gain further insight into these structural changes and to provide an effective coordination number. Overall, it is clear that the network of Si atoms is predominantly 12-coordinate (icosahedral) at any given temperature. However, below T_g, the probability density of the volumes of the Voronoi polyhedra splits (Fig.5(b)), corresponding to the emergence of specific structural features. These can be identified (Fig.5(c)) as defective truncated octahedra consistent with BCC-lattice order as well as polyhedra with 16 and 15 faces unique to the glassy state. In addition, there is a decisive increase in the number of 3 and even 4-membered clusters indicative of the formation of the over-coordinated structures that can be inferred from Figure 5(a) and Figure 5(b).

Below T_g the self-diffusion of the system is so slow that it is possible to relate the power spectrum of the system to specific polyhedra. It is found that the high-frequency region of the power spectra is mostly linked to the polyhedra with 16 faces (Figure 5(d)) at 90 K. Thus, the increase in the local coordination may be part responsible for the blueshift of the OKE spectra on cooling.

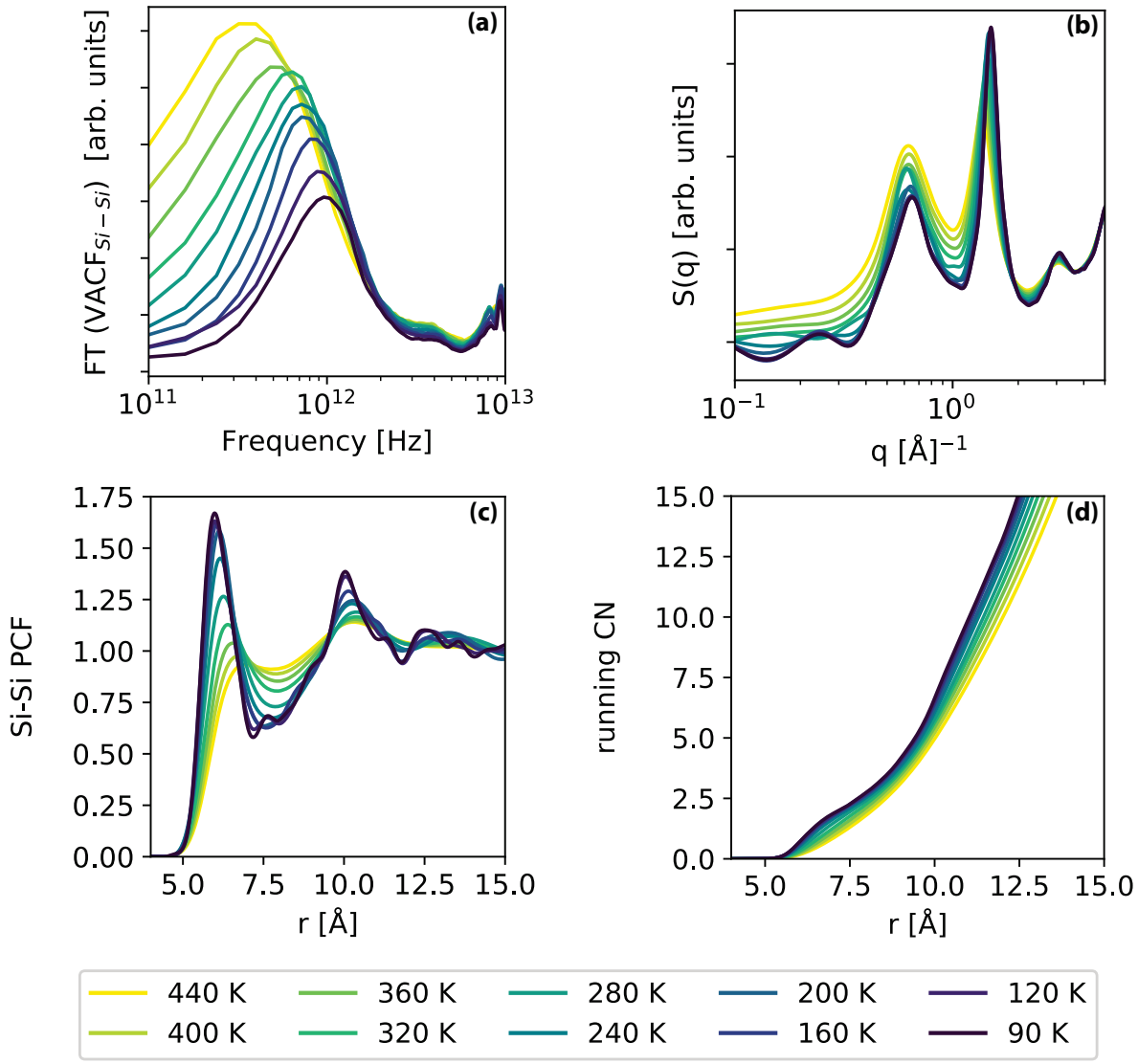

Figure 4. Results of the temperature-dependent molecular-dynamics simulations of TBOS. (a) Power spectra obtained from the Fourier transform of the Si-Si velocity-velocity autocorrelation functions; (b) Static structure factor. The region shaded in green highlights the emergence of the pre-peak observed experimentally (see Figure 3(a)) below the glass transition; (c) Si-Si pair correlation functions; (d) running Si-Si coordination number.

Low-temperature calorimetry. Supplementary Figure 13 shows the specific heat and its Debye representation C_p/T^3 measured using adiabatic and relaxation calorimetry (See Methods). The specific heat curves exhibit a maximum in the C_p/T^3 representation at 6K corresponding to the boson peak.

Discussion and conclusions

Because of the near tetrahedral symmetry of TBOS and hence the nearly isotropic molecular polarisability, no orientational relaxation or librational motions are observed in the OKE spectra. This does not mean that the molecules do not orientationally relax or librate but simply that these processes are not observed here. The lowest frequency relaxational component in the spectra is therefore due to translational relaxation (in as far as rotational and translational motions can be disentangled) and becomes visible in the spectra through a collision-induced process.[18–20]

Apart from the translational relaxation, there are no further relaxational processes observed in TBOS suggesting an absence of β relaxations. However, the lowest observable frequency in these OKE experiments is 10 GHz, whereas β relaxations are typically observed near the glass transition and at much lower (~1 kHz) frequencies.[2,3] Therefore, the presence of β relaxations in TBOS cannot be ruled out. Similarly, a breakdown of the Stokes-Einstein law for translational relaxation much nearer the glass transition could also not be ruled out.

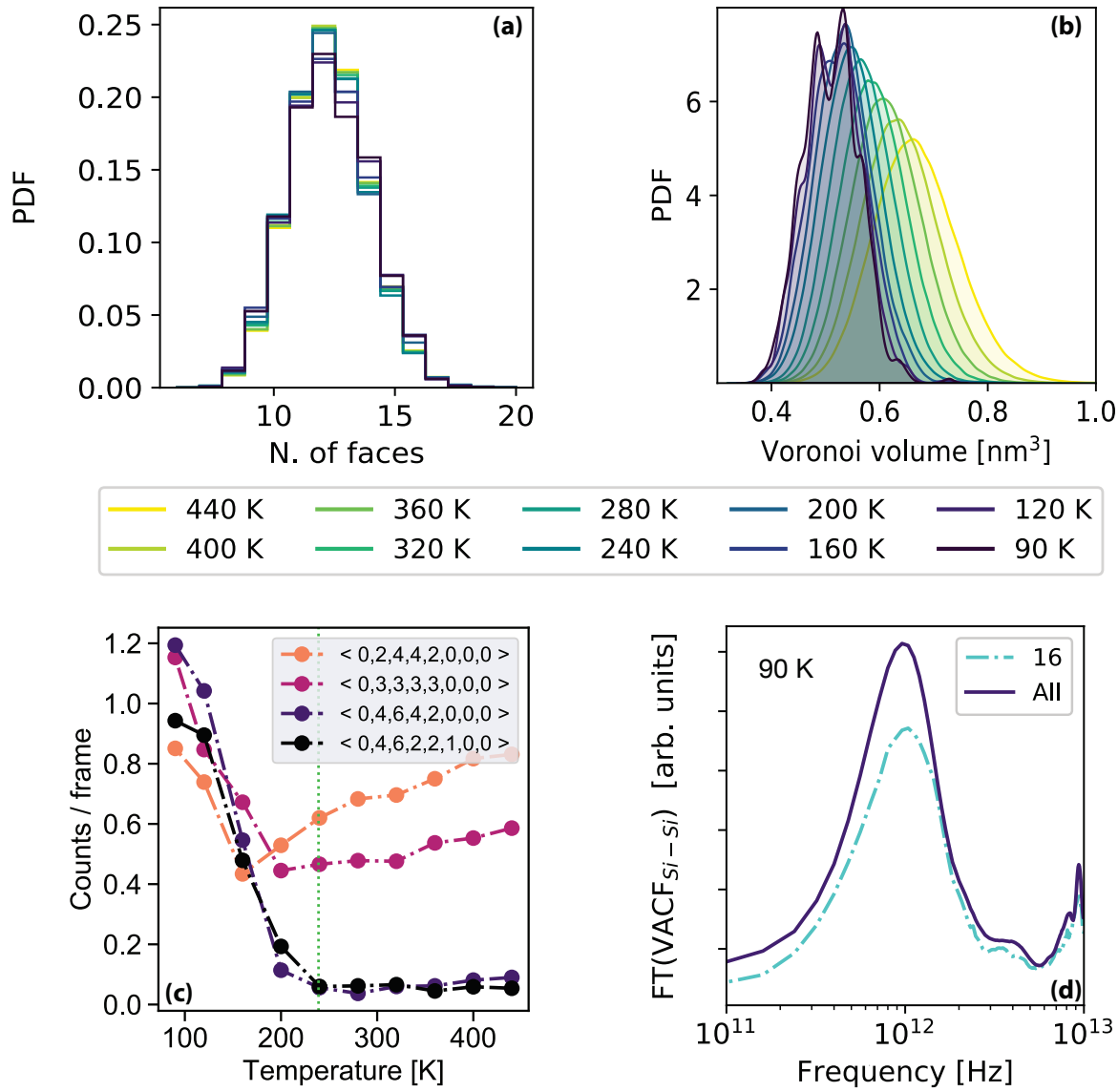

Figure 5. Temperature-dependent Voronoi analysis of TBOS models. (a) Probability density function of the number of faces characterising the Voronoi polyhedra (VP) for each Si atom, averaged over 1000 frames across a 20 ns long MD trajectory. (b) Probability density function of the volume of the VP. (c) Frequency of the occurrence of selected VP indices as a function of temperature. The indices <0,2,4,4,2,0,0,0> and <0,3,3,3,3,0,0,0> correspond to BCC-lattice-like defective truncated octahedra while <0,4,6,4,2,0,0,0> and <0,4,6,2,2,1,0,0>, characterised by 16 and 15 faces, are unique to the glassy state. The green dotted line indicated the value of (computationally obtained) T_g. (d) Power spectra obtained from the Fourier transform of the Si-Si velocity-velocity autocorrelation functions at 90 K. The purple and light blue lines refer to the result obtained considering all the Si atoms (same as Figure 4(a)) and those Si atoms characterised by VP with 16 faces only, respectively.

Because of the near isotropic polarisability tensor of TBOS, the intermolecular band is also collision induced.[18–20] This band is therefore sensitive to transverse and longitudinal motions involving neighbouring molecules and hence to acoustic phonon-like modes near the pseudo Brillouin-zone edge. Therefore, it is tempting to assign the two bands to the LA and TA phonons at the zone edge. However, these would be expected to have similar frequencies (as opposed to a ratio of ~2) and amplitudes (as opposed to a ratio of ~8), while evolving similarly as a function of temperature.[18–20] Therefore, the data are consistent with one of the two bands originating in acoustic phonons at the zone edge with the other one having a different origin.

The absolute amplitude of the intermolecular modes has limited physical relevance as these bands are collision induced and their amplitude therefore reflects the (isotropic) molecular polarisability involved in making them visible through the dipole-induced-dipole effect.[20,39] However, the (temperature dependent) amplitude *ratio* is physically relevant and shows that the low-frequency mode doubles in relative strength on cooling TBOS towards the glass transition. This behaviour is what one might expect for a boson peak, which reflects the additional vibrational density of states due to disorder that is frozen in during vitrification.[1] Hence, we assign the low frequency intermolecular band as the boson peak and the high frequency band as the acoustic phonon band at the pseudo Brillouin zone edge.

Both intermolecular modes in TBOS are inhomogeneously broadened into Gaussian lineshapes. The width of the acoustic phonon band shows no temperature dependence consistent with it representing the inhomogeneity of the liquid state. The width of the boson peak increases on cooling (down to ~200 K) representing an increase in the inhomogeneity on cooling. It may be surmised that the boson peak's lower (collision-induced) amplitude, lower frequency, and more rapidly changing frequency and width, are all associated with the formation of clusters of TBOS molecules undergoing collective oscillation.

The first sharp diffraction peak in the WAXS data is inhomogeneously broadened to a Gaussian consistent with the shape of the acoustic phonon band seen in OKE. At temperatures below the glass transition a pre-peak emerges with a peak at 0.234 $Å^{-1}$ corresponding to a distance of 26.9 Å. This demonstrates the presence of supramolecular clusters in the glass approximately 2.7 TBOS molecules across or about 20 molecules in total. Although there is no incontrovertible proof, it is reasonable to conclude that this pre-peak has the same origin as the boson peak in the OKE spectra.

The atomistic MD simulations also reveal a low-q peak at 0.25 $Å^{-1}$, while reproducing the key features of the OKE spectra and WAXS data. While it is not possible to make a quantitative connection with the supramolecular structures associated with the boson peak identified by OKE measurements (even slower cooling rates and even larger models would be needed), the MD simulations are strongly suggestive that these structures are clusters of over-coordinated TBOS molecules which—were it not for the presence of the long side chains on top of the tetrahedral Si—would tend toward a BCC-like structural order.

@@@It would be nice if C_p/T^3 also were to show a peak at the same frequency and where we do not have to apply a fudge factor as done previously.[9]

We have shown here that symmetry can be used to simplify depolarised Raman spectra to bring out the intermolecular modes. In TBOS, one of these modes is fully consistent with a boson peak, which is present throughout the (supercooled) liquid range but becomes stronger and more easily visible on vitrification. Molecular dynamics simulations and WAXS data show that the boson peak feature is related to clusters of over-coordinated TBOS molecules consisting of circa 20 molecules that are prevented from attaining crystalline structure. Calorimetry.

TBOS is representative of a broad class of molecular liquids consisting of alkoxides of early transition metals and group 14 elements of technological significance in which symmetry can be utilised to simplify Raman and infrared spectra while showing the full range of complexity of glass-forming liquids and crystal nucleation. By changing the metal or the ligand, the symmetry and strength of intermolecular interaction can be changed freely making these liquids of enormous interest for fundamental studies of nucleation and vitrification. Thus, this opens the way to the investigation of the detailed changes in the behaviour of boson-peak as a function of temperature, pressure, fragility, and other physicochemical parameters, greatly aiding the science of the glassy state.

Methods

Sample preparation. TBOS purchased from Aldrich Chemistry and has a rated purity ≥ 97 % and was used without further purification. Liquid samples were filtered with a PTFE filter (Millex) with 20 μm pore size and degassed for 1 min in an ultrasound bath before measurements. Room-temperature samples were contained in a 1 mm thick rectangular quartz cuvette (Starna) and held in a temperature-controlled (±0.5 K) aluminium block. Low-temperature measurements were performed using a liquid-N_2 cryostat (Oxford Instruments, ±0.1 K) in a nitrogen environment to avoid water condensation.

OKE experimental details. A laser oscillator (Coherent Micra) produced ~ 10 nJ pulses at a repetition rate of 82 MHz and with 800 nm nominal wavelength providing 20 fs temporal pulse width in the sample, broadening to 25 fs when using a cryostat. The OKE data were recorded in a standard time-domain pump-probe configuration and Fourier transformed to obtain the frequency-domain reduced depolarised Raman spectrum as described previously.[40] The data were analysed through curve fitting as described in Supplementary note 1.

SAXS and WAXS experiments. Small and wide-angle x-ray scattering (SAXS/WAXS) experiments were carried out at the Diamond Light Source (Oxford) at beam line I22 using Pilatus P3-2M (SAXS) and Pilatus P3-2M-L (WAXS) detectors and using an x-ray wavelength of 1 Å.[41] Liquid samples were contained in sealed plastic capillaries and inserted into a Linkam capillary stage allowing the temperature to be controlled between -180°C and +550°C with an accuracy of ±0.1°C. The experiments were carried out by ramping down the temperature at a rate of 10 K/minute and taking SAXS/WAXS data at 2 K intervals (400 ms averaging time).

The background SAXS/WAXS signal from the capillary, air, and vacuum window was subtracted and the data processed using Dawn to give the intensity $I(q)$ of the scattered x-rays. The experimental structure factor was calculated using[42]

$$S(q) = \frac{I(q)}{f^2(q)} = S_{coh}(q) + f^2(q) S_{incoh}(q), \quad (1)$$

where the atomic structure factor $f(q)$ was approximated using Gaussian functions with tabulated parameters.[43] The incoherent scattering contribution was then

calculated[44] and its amplitude determined by fitting $S(q)$, thereby avoiding having to use the Krogh-Moe-Norman method.[42] However, it was found that the incoherent contribution was negligible in the range studied and hence it was ignored in order to improve the stability of the fitting procedure. The data were analysed through curve fitting as described in Supplementary note 2.

Molecular dynamics simulations. The all-atom CHARMM36 force field[45] (version jul2017) was used to model the TBOS molecules. The relevant parametrisation was obtained via CGenFF (penalties).[46] Despite the lack of explicit refinement of the resulting force-field parameters, the computational results are in good agreement with the experimental measurements with respect to both structural and dynamical properties (see Figure 4 and Figure 5).

The GROMACS package (version 2021)[47] was used to perform molecular dynamics simulations within the NPT ensemble. A leap-frog algorithm[48] was used to integrate Newton's equations of motion with a 2-fs time step. A twin cut-off of 12 Å was used for both electrostatic and van der Waals interactions, where, for the latter, forces were smoothly switched to zero between 10 and 12 Å. The Bussi-Donadio-Parrinello thermostat[49] was used to sample the canonical ensemble, in conjunction with the Berendsen barostat.[50] The coupling constants for the thermostat and barostat are 1.0 and 4.0 ps, respectively. The LINCS[51] algorithm was used to constrain the TBOS bonds involving hydrogen atoms.

In order to generate models of TBOS at different temperatures, 512 TBOS molecules were positioned at random positions within a cubic box. The system was then slowly equilibrated in terms of both temperature and pressure at 440 K and 1 bar. In this regime, the self-diffusion is sufficient to sample a reasonable portion of the configurational space for the liquid phase, thus providing an adequate starting point for the cooling ramp. The latter was implemented as a linear ramp, from 440 K to 90 K at 0.32×10^9 K/s. Configurations generated at temperature intervals of 30 K along the ramp were used as starting points for a 20-ns equilibration at that particular temperature. The system was also annealed from 90K to 440 K in the same fashion, obtaining a discrepancy in the T_g of only 7 K. The lack of significant hysteresis is a strong indicator of the adequacy of the computational protocol.

The static structure factors reported in Figure 4(b) were obtained according to widely used expression reported in, *e.g.*, Eq. (6) in Ref. [52]. The x-ray atomic form factors were constructed from the relevant empirical constants[52] that can be found in the International Tables for Crystallography.[43]

The power spectra reported in Figure 4 and Figure 5 were obtained from 25 ps (sampled every 2 fs) sections of MD trajectory taken from the 20 ns long equilibration runs at each temperature.

To perform the Voronoi analysis, the VORO++ library[53] was used.

Differential scanning calorimetry. Differential scanning calorimetry measurements were carried out with a TA Instruments DSC 2500 differential scanning calorimeter equipped with a Quench Cooling Accessory. The samples were cooled from 40°C with liquid nitrogen in circa 16 minutes to a temperature of -165°C.

Low-temperature calorimetry. Measurements of the specific heat, C_p, from 1 K up to room temperature were taken. The measurements were carried out with a Quantum Design physical properties measurement system (PPMS) relaxation-type calorimeter employing a ^{3}He probe in the temperature range $1\ K \leq T \leq 20\ K$. In addition, specific heat measurements were performed from 10 to 300 K using an adiabatic calorimeter.[54] Resolutions of the measurements are 0.3% for the relaxation calorimetry and 0.2% for the adiabatic calorimetry.

FTIR. Fourier-transform infrared (FTIR) spectroscopy measurements used a Bruker Vertex 70 spectrometer purged with dry air. liquid samples were sandwiched between two ZnSe windows. Sub-ambient FTIR experiments were performed using the same liquid-N_2 cryostat with ZnSe windows.

NMR. Temperature-dependent ^{13}C magic-angle spinning (MAS) NMR spectra were recorded on a 400 MHz Bruker ASCEND NEO spectrometer equipped with a 4 mm Bruker CPMAS probe. The investigated liquids were closed into Kel-F inserts before being put into 4 mm zirconia rotors. During the measurements, the samples were spun with frequencies of up to 10 kHz. A 90° pulse of 3.8 µs was used for the excitation of carbon nuclei, and proton decoupling was employed during signal acquisition. The number of scans was 256 using a repetition delay of 3 s. The ^{13}C shifts were reported relative to the position of the ^{13}C signal of tetramethylsilane (TMS).

Raman. Confocal Raman microscopy experiments were performed using a Horiba LabRAM HR confocal microscope system. The excitation source was a vertically polarised 28-mW frequency-doubled DPSS laser operating at 532 nm. Temperature was controlled to ±0.1 K using a Linkam THMS600 microscope stage.

Viscometry. Variable temperature storage (G') and loss (G'') modulus measurements were performed on an Anton Paar MCR 702e rheometer using a 50-mm cone (cone angle = 1°, gap = 0.101 mm) using a 10-Hz shear frequency. The loss tangent and complex viscosity were calculated from these data. The temperature was lowered from 40°C to -160°C at a rate of 1°C/min and the data recorded every minute.

Molecular and normal mode calculations. While full conformational analysis of the TBOS molecule is beyond the scope of this study, it is still useful to estimate differences in dipole moment and polarisability for various conformers. In order to achieve that, low-energy conformers were generated using Confab algorithm[55] yielding more than 31,500 conformers. 100 structures were then picked randomly to form a subset for subsequent DFT optimisations and property calculations.

All DFT calculations were performed using the ORCA 4.2.1 quantum chemistry program.[56] Geometry optimisations and vibrational spectra calculations were carried out with the ωB97X-D3 exchange-correlation functional[57] combined with ma-def2-SVP basis set.[58] Solvent effects were not accounted for. RIJCOSX approximation with default cut-offs was used for all DFT calculations. IR and depolarised Raman spectra for separate conformers were obtained in the double harmonic approximation. Spectra were broadened with Lorentzians with 12 cm^{-1} half-width and averaged using Boltzmann weights.

For all 100 conformers polarisability tensors were computed and a mean and standard deviation for iso- and anisotropic polarisabilities as well as dipole moment were estimated (see Figure 6 and Table 1). It is worth noting that mean and standard deviation are unweighted, that is, each conformer contributed equally, which partially accounts for the relatively small sample size. For the anisotropic polarisability, the values are approximately an order of magnitude smaller than for the isotropic polarisability. Also, the relative SDs are comparable and large for the dipole moment and anisotropic polarizability as both are very sensitive towards changes in dihedrals for this molecule.

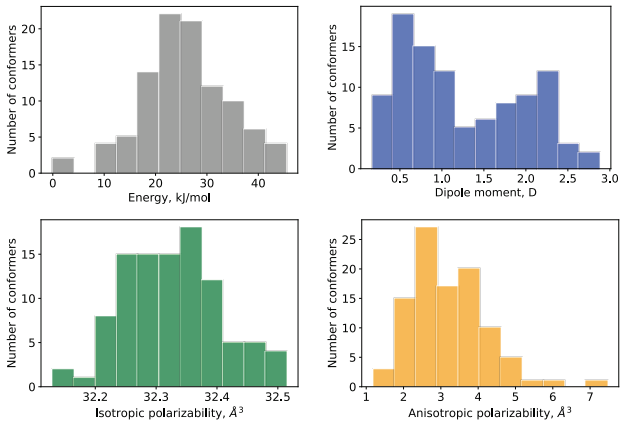

Figure 6. Histograms for various properties estimated for 100 TBOS conformers.

Table 1. *Dipole moment and polarisability statistics for TBOS conformers (mean and standard deviation).*

μ / D	α_{iso}, Å^3	α_{aniso}, Å^3
1.25±0.71	32.3±0.1	3.2±1.0

Silicon alkoxide aggregation. Recent work has shown that in some cases organosilicates can aggregate to form molecular structures with an octahedral SiO_6 motif.[59,60] To ensure that simple silicon alkoxides remain monomeric under normal conditions, the stability of a dimer and various trimers (see Figure 7) were investigated by means of DFT calculations for prototypical $Si(OMe)_4$. It was found that, with the exception of the dimer and trimer **II**, the formation of aggregates is enthalpically favourable; however, due to the decrease of entropy associated with forming a cluster, the Gibbs free energies are clearly positive for all structures considered (Table 2). Since the formation of higher order aggregates would impose even larger entropy penalty, silicon alkoxides can be assumed to remain monomeric under normal conditions.

Table 2. *Formation energies (in kJ/mol , per 1 mole of monomer) for the dimer and various trimers (**I-IV**) of $Si(OMe)_4$.*

	dimer	trimers			
		I	**II**	**III**	**IV**
ΔE	4	-13	9	-6	-22
ΔH_{298}	5	-11	13	-3	-18
ΔG_{298}	39	39	64	45	32

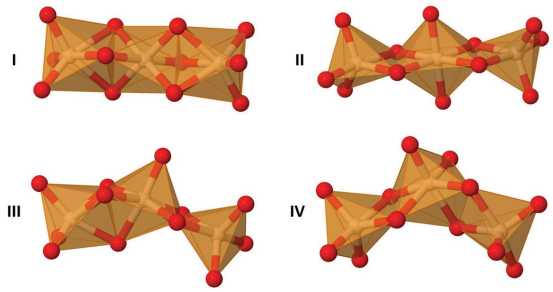

Figure 7. SiO skeletons for different minima on $Si_3(OMe)_{12}$ potential energy surface.

Data availability

The data that support the findings of this study are available in Enlighten: Research Data Repository (University of Glasgow) with the identifier: http://dx.doi.org/10.5525/gla.researchdata.@@@.

References

1. Angell, C. A., Ngai, K. L., McKenna, G. B., McMillan, P. F. & Martin, S. W. Relaxation in glassforming liquids and amorphous solids. *J. Appl. Phys.* **88**, 3113–3157 (2000).
2. Hai Bin Yu, Wei Hua Wang, Hai Yang Bai, & Konrad Samwer. β-relaxation in metallic glasses | National Science Review | Oxford Academic. *Natl. Sci. Rev.* **1**, 429–461 (2014).
3. Boyer, R. F. Dependence of mechanical properties on molecular motion in polymers. *Polym. Eng. Sci.* **8**, 161–185 (1968).
4. Ueno, K. & Angell, C. A. On the Decoupling of Relaxation Modes in a Molecular Liquid Caused by Isothermal Introduction of 2 nm Structural Inhomogeneities. *J. Phys. Chem. B* **115**, 13994–13999 (2011).

5. Johari, G. P. Source of JG-Relaxation in the Entropy of Glass. *J. Phys. Chem. B* **123**, 3010–3023 (2019).
6. Johari, G. P. Localized molecular motions of β-relaxation and its energy landscape. *J. Non-Cryst. Solids* **307–310**, 317–325 (2002).
7. Tanaka, H. Origin of the excess wing and slow β relaxation of glass formers: A unified picture of local orientational fluctuations. *Phys. Rev. E* **69**, 021502 (2004).
8. Parshin, D. A., Schober, H. R. & Gurevich, V. L. Vibrational instability, two-level systems, and the boson peak in glasses. *Phys. Rev. B* **76**, 064206 (2007).
9. Alvarez-Ney, C., Labarga, J., Moratalla, M., Castilla, J. M. & Ramos, M. A. Calorimetric Measurements at Low Temperatures in Toluene Glass and Crystal. *J. Low Temp. Phys.* **187**, 182–191 (2017).
10. Schirmacher, W., Ruocco, G. & Scopigno, T. Acoustic Attenuation in Glasses and its Relation with the Boson Peak. *Phys. Rev. Lett.* **98**, 025501 (2007).
11. Taraskin, S. N., Loh, Y. L., Natarajan, G. & Elliott, S. R. Origin of the Boson Peak in Systems with Lattice Disorder. *Phys. Rev. Lett.* **86**, 1255–1258 (2001).
12. Lerner, E. & Bouchbinder, E. Low-energy quasilocalized excitations in structural glasses. *J. Chem. Phys.* **155**, 200901 (2021).
13. Shintani, H. & Tanaka, H. Universal link between the boson peak and transverse phonons in glass. *Nat. Mater.* **7**, 870–877 (2008).
14. Tanaka, H. Two-order-parameter model of the liquid–glass transition. III. Universal patterns of relaxations in glass-forming liquids. *J. Non-Cryst. Solids* **351**, 3396–3413 (2005).
15. Chumakov, A. I. *et al.* Equivalence of the Boson Peak in Glasses to the Transverse Acoustic van Hove Singularity in Crystals. *Phys. Rev. Lett.* **106**, 225501 (2011).
16. Baggioli, M. & Zaccone, A. Universal Origin of Boson Peak Vibrational Anomalies in Ordered Crystals and in Amorphous Materials. *Phys. Rev. Lett.* **122**, 145501 (2019).
17. Chumakov, A. I. *et al.* Role of Disorder in the Thermodynamics and Atomic Dynamics of Glasses. *Phys. Rev. Lett.* **112**, 025502 (2014).
18. Turton, D. A. & Wynne, K. Universal nonexponential relaxation: Complex dynamics in simple liquids. *J. Chem. Phys.* **131**, 201101 (2009).
19. Reichenbach, J. *et al.* Phonon-like Hydrogen-Bond Modes in Protic Ionic Liquids. *J. Am. Chem. Soc.* **139**, 7160–7163 (2017).
20. Farrell, A. J., González-Jiménez, M., Ramakrishnan, G. & Wynne, K. Low-Frequency (Gigahertz to Terahertz) Depolarized Raman Scattering Off *n*-Alkanes, Cycloalkanes, and Six-Membered Rings: A Physical Interpretation. *J. Phys. Chem. B* **124**, 7611–7624 (2020).
21. Schmid, B. & Schirmacher, W. Raman Scattering and the Low-Frequency Vibrational Spectrum of Glasses. *Phys. Rev. Lett.* **100**, 137402 (2008).
22. Orsingher, L., Baldi, G., Fontana, A. & Rossi, F. The Raman coupling function in permanently densified GeO2 glasses. *Philos. Mag.* **91**, 1857–1863 (2011).
23. Fontana, A. *et al.* The Raman coupling function in amorphous silica and the nature of the long-wavelength excitations in disordered systems. *EPL Europhys. Lett.* **47**, 56 (1999).
24. Achibat, T., Boukenter, A. & Duval, E. Correlation effects on Raman scattering from low-energy vibrational modes in glasses. II. Experimental results. *J. Chem. Phys.* **99**, 2046–2051 (1993).
25. Mantisi, B. *et al.* Non-Debye normalization of the glass vibrational density of states in mildly densified silicate glasses. *J. Phys. Condens. Matter* **22**, 025402 (2010).
26. Cundy, C. S. & Cox, P. A. The Hydrothermal Synthesis of Zeolites: History and Development from the Earliest Days to the Present Time. *Chem. Rev.* **103**, 663–702 (2003).
27. Beck, J. S. *et al.* A new family of mesoporous molecular sieves prepared with liquid crystal templates. *J. Am. Chem. Soc.* **114**, 10834–10843 (1992).
28. Hoffmann, F., Cornelius, M., Morell, J. & Fröba, M. Silica-Based Mesoporous Organic–Inorganic Hybrid Materials. *Angew. Chem. Int. Ed.* **45**, 3216–3251 (2006).
29. Huo, Q., Feng, J., Schüth, F. & Stucky, G. D. Preparation of Hard Mesoporous Silica Spheres. *Chem. Mater.* **9**, 14–17 (1997).
30. Duraiswamy, S. & Khan, S. A. Plasmonic Nanoshell Synthesis in Microfluidic Composite Foams. *Nano Lett.* **10**, 3757–3763 (2010).
31. Bradley, D., Mehrotra, R. C., Rothwell, I. & Singh, A. *Alkoxo and Aryloxo Derivatives of Metals*. (Elsevier, 2001).
32. Oda, S., Kohara, S., Tsutsui, R., Kasasaku, M. & Kozuka, H. Structure and glass transition of amorphous materials composed of titanium-oxo oligomers chemically modified with benzoylacetone. *RSC Adv.* **10**, 15665–15669 (2020).
33. Bender, J. S., Zhi, M. & Cicerone, M. T. The polarizability response of a glass-forming liquid reveals intrabasin motion and interbasin transitions on a potential energy landscape. *Soft Matter* **16**, 5588–5598 (2020).
34. Cang, H., Li, J., Andersen, H. C. & Fayer, M. D. Boson peak in supercooled liquids: Time domain observations and mode coupling theory. *J. Chem. Phys.* **123**, 064508 (2005).
35. Walton, F. *et al.* Polyamorphism Mirrors Polymorphism in the Liquid–Liquid Transition of a Molecular Liquid. *J. Am. Chem. Soc.* **142**, 7591–7597 (2020).
36. Gonzalez-Jimenez, M., Ramakrishnan, G., Tukachev, N. V., Senn, H. M. & Wynne, K. Low-

frequency vibrational modes in G-quadruplexes reveal the mechanical properties of nucleic acids. *Phys. Chem. Chem. Phys.* **23**, 13250–13260 (2021).
37. Farrell, A. *et al.* Characterisation of the Boson Peak from the Glass into the Liquid. (2021) doi:10.26434/chemrxiv.14685924.v1.
38. Lunkenheimer, P., Schneider, U., Brand, R. & Loid, A. Glassy dynamics. *Contemp. Phys.* **41**, 15–36 (2000).
39. Bucaro, J. A. & Litovitz, T. A. Rayleigh Scattering: Collisional Motions in Liquids. *J. Chem. Phys.* **54**, 3846–3853 (1971).
40. Turton, D. A. *et al.* Terahertz underdamped vibrational motion governs protein-ligand binding in solution. *Nat. Commun.* **5**, 3999 (2014).
41. Smith, A. J. *et al.* I22: SAXS/WAXS beamline at Diamond Light Source – an overview of 10 years operation. *J. Synchrotron Radiat.* **28**, 939–947 (2021).
42. Daisenberger, D. *et al.* Polyamorphic Amorphous Silicon at High Pressure: Raman and Spatially Resolved X-ray Scattering and Molecular Dynamics Studies. *J. Phys. Chem. B* **115**, 14246–14255 (2011).
43. Brown, P. J., Fox, A. G., Maslen, E. N., O'Keefe, M. A. & Willis, B. T. M. Intensity of diffracted intensities. in *International Tables for Crystallography* vol. C 554–595 (International Union of Crystallography, 2006).
44. Smith, V. H., Thakkar, A. J. & Chapman, D. C. A new analytic approximation to atomic incoherent X-ray scattering intensities. *Acta Crystallogr. A* **31**, 391–392 (1975).
45. Vanommeslaeghe, K. & MacKerell, A. D. CHARMM additive and polarizable force fields for biophysics and computer-aided drug design. *Biochim. Biophys. Acta BBA - Gen. Subj.* **1850**, 861–871 (2015).
46. Vanommeslaeghe, K. *et al.* CHARMM general force field: A force field for drug-like molecules compatible with the CHARMM all-atom additive biological force fields. *J. Comput. Chem.* **31**, 671–690 (2010).
47. Van Der Spoel, D. *et al.* GROMACS: Fast, flexible, and free. *J. Comput. Chem.* **26**, 1701–1718 (2005).
48. Van Gunsteren, W. F. & Berendsen, H. J. C. A Leap-frog Algorithm for Stochastic Dynamics. *Mol. Simul.* **1**, 173–185 (1988).
49. Bussi, G., Donadio, D. & Parrinello, M. Canonical sampling through velocity rescaling. *J. Chem. Phys.* **126**, 014101 (2007).
50. Berendsen, H. J. C., Postma, J. P. M., van Gunsteren, W. F., DiNola, A. & Haak, J. R. Molecular dynamics with coupling to an external bath. *J. Chem. Phys.* **81**, 3684–3690 (1984).
51. Hess, B., Bekker, H., Berendsen, H. J. C. & Fraaije, J. G. E. M. LINCS: A linear constraint solver for molecular simulations. *J. Comput. Chem.* **18**, 1463–1472 (1997).
52. Liu, H. & Paddison, S. J. Direct calculation of the X-ray structure factor of ionic liquids. *Phys. Chem. Chem. Phys.* **18**, 11000–11007 (2016).
53. Rycroft, C. H. VORO++: A three-dimensional Voronoi cell library in C++. *Chaos Interdiscip. J. Nonlinear Sci.* **19**, 041111 (2009).
54. Kume, Y., Mlyazaki, Y., Matsuo, T. & Suga, H. Low temperature heat capacities of ammonium hexachlorotellurate and its deuterated analogue. *J. Phys. Chem. Solids* **53**, 1297–1304 (1992).
55. O'Boyle, N. M., Vandermeersch, T., Flynn, C. J., Maguire, A. R. & Hutchison, G. R. Confab - Systematic generation of diverse low-energy conformers. *J. Cheminformatics* **3**, 8 (2011).
56. Neese, F. The ORCA program system. *WIREs Comput. Mol. Sci.* **2**, 73–78 (2012).
57. Lin, Y.-S., Li, G.-D., Mao, S.-P. & Chai, J.-D. Long-Range Corrected Hybrid Density Functionals with Improved Dispersion Corrections. *J. Chem. Theory Comput.* **9**, 263–272 (2013).
58. Zheng, J., Xu, X. & Truhlar, D. G. Minimally augmented Karlsruhe basis sets. *Theor. Chem. Acc.* **128**, 295–305 (2011).
59. Jähnigen, S., Brendler, E., Böhme, U., Heide, G. & Kroke, E. Silicophosphates containing SiO6 octahedra – anhydrous synthesis under ambient conditions. *New J. Chem.* **38**, 744–751 (2014).
60. Roeser, J. *et al.* Anionic silicate organic frameworks constructed from hexacoordinate silicon centres. *Nat. Chem.* **9**, 977–982 (2017).
61. Cho, M., Du, M., Scherer, N. F., Fleming, G. R. & Mukamel, S. Off-resonant transient birefringence in liquids. *J Chem Phys* **99**, 19 (1993).
62. Mizuguchi, T., Tatsumi, S. & Fujiwara, S. Icosahedral order in liquid and glassy phases of cyclohexane. *Mol. Simul.* **46**, 721–726 (2020).
63. Fukunaga, T. *et al.* Voronoi Analysis of the Structure of Ni-Zr-Al Ternary Metallic Glass. *Mater. Trans.* **48**, 1698–1702 (2007).
64. Brostow, W., Chybicki, M., Laskowski, R. & Rybicki, J. Voronoi polyhedra and Delaunay simplexes in the structural analysis of molecular-dynamics-simulated materials. *Phys. Rev. B* **57**, 13448–13458 (1998).
65. Yannopoulos, S. N., Andrikopoulos, K. S. & Ruocco, G. On the analysis of the vibrational Boson peak and low-energy excitations in glasses. *J. Non-Cryst. Solids* **352**, 4541–4551 (2006).
66. Deschamps, T., Martinet, C., de Ligny, D., Bruneel, J. L. & Champagnon, B. Low-frequency Raman scattering under high pressure in diamond anvil cell: Experimental protocol and application to GeO_2 and SiO_2 boson peaks. *J. Non-Cryst. Solids* **358**, 3156–3160 (2012).
67. Schroeder, J. *et al.* Raman scattering and Boson peaks in glasses: temperature and pressure effects. *J. Non-Cryst. Solids* **349**, 88–97 (2004).
68. Weeraman, C., Yatawara, A. K., Bordenyuk, A. N. & Benderskii, A. V. Effect of Nanoscale Geometry on Molecular Conformation: Vibrational Sum-

Frequency Generation of Alkanethiols on Gold Nanoparticles. *J. Am. Chem. Soc.* **128**, 14244–14245 (2006).
69. Brown, K. G., Bicknell-Brown, Ellen. & Ladjadj, Meriem. Raman-active bands sensitive to motion and conformation at the chain termini and backbones of alkanes and lipids. *J. Phys. Chem.* **91**, 3436–3442 (1987).

Acknowledgments

KW acknowledges funding by a grant from the European Research Council (ERC) under the European Union's Horizon 2020 research and innovation program (grant agreement No. 832703) and by Leverhulme Trust Research Project Grant RPG-2018-350. We thank the Diamond Light Source for access to beamline I22 to carry out SWAXS experiments (proposal number SM27885 and SM28529). KW thanks the Engineering and Physical Sciences Research Council (EPSRC) for support through grants EP/J009733/1, EP/K034995/1, EP/N508792/1, and EP/N007417/1. GM acknowledges financial support from the Slovenian Research Agency (research core funding No. P1-0021). TB thanks the EPSRC for a studentship through the Centre for Doctoral Training in Mathematics for Real-World Systems II (EP/S022244/1). TB and GCS also gratefully acknowledge the use of SULIS, which was funded by the EPSRC (EP/T022108/1), via the HPC Midlands+ Consortium. TB and GCS would also like to acknowledge the high-performance computing facilities provided by the Scientific Computing Research Technology Platform at the University of Warwick.

Author contributions

All authors contributed to the study and manuscript. MGJ was responsible for OKE data collection and their analysis. TB and GCS were responsible for the molecular-dynamics simulations and their analysis. The SAXS/WAXS data were collected by BAR, MGJ, and KW aided by AJS. NVT and HMS were responsible for the DFT calculations of vibrational spectra and molecular polarisabilities. AJF and SG investigated a range of symmetric-molecule liquids for suitability in this study, and carried out initial OKE and FTIR measurements. BAR was responsible for DSC and rheometry measurements. BAR and LAH took the temperature dependent Raman spectra. UJ and GM carried out the solid-state NMR measurements. MK and YM were responsible for the low-temperature calorimetry. MGJ, TB, BAR, NVT, MW, YM, PMcM, GCS, and KW carried out data analysis and manuscript preparation.

Competing interests

The authors declare no competing interests.

Additional information

Additional information is linked to the online version of the paper at www.nature.com/nature.

Corresponding authors

Gabriele C. Sosso – University of Warwick, Department of Chemistry, Coventry CV4 7AL, UK; email: G.Sosso@warwick.ac.uk
Klaas Wynne – University of Glasgow, School of Chemistry, Glasgow G12 8QQ, UK; email: klaas.wynne@glasgow.ac.uk

Supplementary information

Supplementary notes

Supplementary note 1
OKE data analysis.

OKE spectra consist of a number of broad overlapping bands that are either overdamped or underdamped, which are analysed through curve fitting to the imaginary part of a number of analytical complex functions. The overdamped or diffusive mode is fit to the imaginary part of the Havriliak-Negami function, which is defined in the frequency domain by

$$H_{\alpha,\beta}(\omega) = \frac{1}{\left(1+\left(-i\omega\tau\right)^{\alpha}\right)^{\beta}}, \qquad (2)$$

with $0 < \alpha,\beta \leq 1$ and where ω is the angular frequency and τ is the relaxation time. For $\beta = 1$, it reduces to the Cole-Cole function; for $\alpha = 1$ it reduces to the Cole-Davidson function; and for $\alpha = \beta = 1$ it reduces to the Debye function.

However, it would be unphysical if diffusive processes were to be faster than the corresponding underdamped motion. So, diffusive translational relaxation ought to be slower than intermolecular cage-rattling modes. This inertial effect is accommodated using a rise function in the time-domain as described previously.[19] Thus, translational relaxation is fit with an "inertial" Havriliak-Negami function defined by

$$S_{iCD}(\omega) = \mathrm{Im}\left[H_{1,\beta}(\omega) - H_{1,\beta}(\omega + i\gamma_{rise})\right], \qquad (3)$$

where γ_{rise} is the approximate frequency of the intermolecular mode.

In the terahertz range, one finds bands from modes that are not diffusive but critically damped or underdamped. These originate in librations, vibrations, and phonon-like modes. These were fitted using the Brownian oscillator function[40,61]

$$S_{BO}(\omega) = \mathrm{Im}\frac{\omega_0^2}{\omega_0^2 - \omega^2 - i\gamma\omega}, \qquad (4)$$

where ω_0 is the undamped oscillator angular frequency and γ is the damping rate. For the intermolecular modes, it is required to take into account inhomogeneous broadening and the bands are fitted using the antisymmetrised Gaussian function defined by

$$S_G(\omega) = \frac{1}{\sigma\sqrt{2\pi}}\left[e^{-\frac{(\omega-\omega_0)^2}{2\sigma^2}} - \mathrm{e}^{-\frac{(\omega+\omega_0)^2}{2\sigma^2}}\right] \qquad (5)$$

where σ is a width parameter.

The parameters of these functions, listed in Supplementary Table 1, were adjusted using the following procedure. Initially, it was determined that the minimum number of functions needed to describe the spectra in the range between 1 GHz and 10 THz was one inertial Havriliak-Negami, two antisymmetrised Gaussian, and 5 Brownian functions. Each experimental OKE spectrum was then fitted independently following a random sequence of temperatures to avoid systematic errors. For each fit, the parameters of a previous randomly selected fit were used as initial values.

When leaving all the fit parameters free to change, the amplitude of the Brownian oscillator (peaking at *circa* 3 THz) stays constant within the accuracy of the data, consistent with it being an intramolecular mode. In subsequent fitting, its amplitude was set to be constant. Similarly, the parameter τ_{rise} of the inertial Havriliak-Negami function remained constant at temperatures above 200 K, so it too was fixed during the fits.

The rest of the parameters were not fixed. The validity of the fits was subsequently checked by evaluating their change with temperature, which could be linear as in Figure 1(d), exponential as in Figure 2 or, in the case of the translational-relaxation time, following the Stokes-Einstein expression (Supplementary Figure 7).

Supplementary note 2
Analysis of WAXS data

The WAXS data can be fitted with two analytical functions, a Lorentzian

$$L(q) = \frac{\gamma/\pi}{\gamma^2 + \left(q - q_0\right)^2}, \qquad (6)$$

and a Gaussian

$$G(q) = \frac{1}{\sqrt{2\pi}\sigma}\exp\left(-\frac{\left(q-q_0\right)^2}{2\sigma^2}\right), \qquad (7)$$

both of which are normalised by area. A total of 4 Gaussians and 1 Lorentzian were required to fit the WAXS data giving the fit function

$$S(q) = G_3(q) + G_4(q) + L_5(q) + G_6(q) + G_7(q). \qquad (8)$$

The pair-distribution function is calculated from the fit functions using[42]

$$g(r) = 1 + \frac{1}{2\pi^2 r\rho_0}\int_0^{\infty} q\left[S(q) - 1\right]\sin(qr)\,dq. \qquad (9)$$

The SAXS data additionally required a Porod function for the low q region

$$P(q) = \frac{10^{-2n}}{q^n} \qquad (10)$$

as well an additional Gaussian for the boson peak, giving the fit function

$$S(q) = P_1(q) + G_2(q) + G_3(q) + G_4(q) + L_5(q) + G_6(q) + G_7(q) + G_8(q) \quad (11)$$

Supplementary note 3
Details of MD simulations and Voronoi analysis

Via atomistic MD simulations (see the Methods section for the computational details), a 512-molecule model of liquid TBOS was generated, which was quenched (at a rate of 3.2×10^8 K/s) into the glass. The resulting T_g, obtained from the thermal expansion data reported in Supplementary Figure 12 is 249±20 K. It should be noted that this value is significantly higher than its experimental counterpart (124 K). However, it is expected for the simulations to overestimate T_g due to the much faster cooling rate. The MD data reported hereafter refer to 20 ns long simulations performed at a given temperature within the NPT ensemble.

The Fourier transform of the Si-Si velocity-velocity autocorrelation function (see the Methods section for the computational details) should display similar trends to the OKE signal measured experimentally, due to the symmetry considerations discussed in the previous section. Indeed, the results reported in Figure 4(a) are in good agreement with the experimental data, particularly in terms of the decrease of the intensity of signal upon cooling as well as the shift of the signal to higher frequencies upon cooling.

Moving on to the structural features of TBOS, the MD simulations identified the emergence of a low-q feature within the total (static) structure factor, reported in Figure 4(b) – thus providing further evidence for the pre-peak observed experimentally, see Figure 3(a). This pre-peak was observed in a 216-molecule model of TBOS as well (generated following the exact same computational protocol), however to a lesser extent—likely because of the fact that this feature corresponds in subtle structural changes spanning ~25 Å in real space—hence the need for a large-enough TBOS model. A comparison between the total (static) structure factor obtained for the 216- and 512-molecule models is reported in Supplementary Figure 12.The partial (static) structure factors, obtained for every other atomic species in the system (as opposed to Si only, and we the exception of hydrogen atoms) are reported in Supplementary Figure 14.The structural changes are even more evident in the Si-Si pair correlation function reported in Figure 4(c). It is interesting to observe the significant increase in terms of short-range order, particularly as it concerns the second coordination shell. In fact, the running coordination number reported in Figure 4(d) provides further insight into the topology of the TBOS network. The first coordination shell (which extends up to ~6 Å) only contains, on average, about 2 molecules – which shows the lack of tetrahedral order in both liquid and glassy TBOS. However, the second coordination shell (which extends up to ~12 Å) contains about 12 molecules – a number that appears to monotonically, if slightly, increase upon cooling. The pair correlation functions obtained for every other atomic species in the system (as opposed to Si only, and we the exception of hydrogen atoms) are reported in Supplementary Figure 15.

To gain further insight into these structural changes and attempt to link them to the dynamical properties highlighted by the OKE measurements, a Voronoi analysis was performed (see the Methods section for further computational details), which, amongst other aspects, provides an "effective" coordination number whose definition does not depend on the choice of any specific cut-off radius. In the context of e.g. metallic alloys, the Voronoi Polyhedron (VP) corresponding to any given atom is usually labelled[62] in terms of Schläfli notation via a tuple of four indices as $<n_3, n_4, n_5, n_6>$, where n_i refers to the number of faces with i vertexes (or, equivalently, edges) within that particular VP. However, it was found that the complexity of the TBOS network is such that a more extensive indexing is required, namely $<n_3, n_4, n_5, n_6, n_7, n_8, n_9, n_{10}>$, to fully appreciate the topology of the system. This indexing has been used before when dealing with complex molecular systems displaying a huge variety of VP.[63] However, the overwhelming majority of VPs observed is characterised by $n_9 = n_{10} = 0$.

We start by investigating the distribution of the total number of faces characterising each VP. To this end, 1,000 configurations were considered of the TBOS model at any given temperature, across a 20 ns long MD simulation. The total number of faces corresponds to the effective coordination number of any given *j*-th Si atom (the only species considered for the Voronoi analysis), as $CN_j = \sum_{i=1}^{10} n_i$. To reduce the complexity of the Voronoi analysis, faces that account for less than 1% of the total surface area of a given VP were ignored—in line with the approach of, *e.g.*, Ref. [64] —aimed at avoiding overcounting and remove too small structural fluctuations.

The results are reported, as a function of temperature, in Figure 5(a). Overall, it is clear that the network of Si atoms within TBOS is predominantly 12-coordinate at any given temperature – albeit relaxing or removing the < 1% criterion in terms of surface area mentioned above substantially increase the coordination number up to 14 or 16, respectively. Whilst the sheer variety of VP indexes (more than 1,000) prevents a quantitative statement about the exact topology of the system, the frequency by which n6 and n7 are observed suggests that TBOS tends toward a BCC-type order, as the VP of both FCC and HCP lattices contain exclusively n4 faces. In fact, the two most frequent VP with 12 faces are the <0,2,4,4,2,0,0,0> and the <0,3,3,3,3,0,0,0> VP, which, if we ignore the < 1% criterion in terms of surface area mentioned above, turn out to be defective truncated octahedra (*i.e.*, the Voronoi cell of a BCC lattice).

It can also be seen that the number of faces of the VP increases on cooling, consistent with the structuring of

the Si-Si PCF illustrated in Figure 4(a). In particular, a proliferation of VP is observed characterised by 13, 14, and even 16 faces below T_g. Even more telling is the distribution of the volumes of the VPs as a function of temperature, reported in Figure 5(b). In this case, a split in the probability density function of said VP volumes can clearly be identified below T_g, which must correspond to the emergence of specific structural features.

It was attempted to pinpoint the latter by looking at the changes of the occurrence of a given VP upon cooling. Figure 5(c) reports a representative selection. The population of the above mentioned <0,2,4,4,2,0,0,0> and <0,3,3,3,3,0,0,0> VP drastically increases below T_g and there are specific VP that are simply unique to the glassy state, such as the <0,4,6,4,2,0,0,0> and <0,4,6,2,2,1,0,0>, characterised by 16 and 15 faces, respectively. In addition, if the most frequent VP at each temperature are clustered together based on a simple distance criterion (see the Methods section for further computational details), a decisive increase in the number of 3 and even 4-membered clusters is observed, which is indicative of the formation of the over-coordinated structures that can be inferred from Figure 5(a) and Figure 5(b).

While it is not possible to make a quantitative connection with the supra-molecular structures identified by means of the OKE measurements (even slower cooling rates and even larger models might be needed to offer a quantitative comparison with the experimental data), the MD simulations are strongly suggestive that these structures are clusters of over-coordinated TBOS molecules which – were if not for the presence of the long side chains on top of the tetrahedral Si – would tend toward a BCC-like structural order.

Finally, as below T_g the self diffusion of the system is so low that the local molecular environments tend to remain unchanged within the 20 ns timescale investigated in our MD simulations (see Supplementary Figure XXX), one can attempt to "project", so to speak, the power spectrum of the system onto specific Si atoms characterised by specific VP. It is found that VPs characterised by 16 faces tend to populate the high-frequency region of the power spectra, as illustrated in Figure 5(d) at 90 K. Therefore, the increase in the local coordination of the TBOS molecules might also be part responsible for the shift of the OKE signal toward higher frequencies upon cooling in addition to the collision-induced effects.

Supplementary note 4
Relation between viscosity and relaxation rate

Translational diffusion is described by the Stokes-Einstein equation, which predicts the translational diffusion coefficient to be given by

$$D_{trans} = \frac{k_B T}{6\pi\eta R} \,. \tag{12}$$

If the temperature-dependent viscosity is described by a Vogel-Fulcher-Tammann equation, one would expect the relaxation time to be proportional to

$$\tau \sim T^{-1} \exp\left(\frac{DT_0}{T - T_0}\right) \,. \tag{13}$$

Supplementary note 4
Density of states and the boson peak

The vibrational density of states (VDoS) $g(\omega)$ can be measured in several related experiments such as Raman scattering (including OKE spectroscopy), inelastic neutron scattering, *etc*. Such spectroscopies often do not measure $g(\omega)$ directly but instead a product of the VDoS with the strength of the coupling associated with the particular spectroscopy. Thus, the various spectroscopies measure the same dynamics or spectra but with different amplitudes for the various components. For example, the spontaneous Raman scattering (SRS) spectrum is related to the VDoS by[65]

$$S^{SRS}(\omega) \propto g(\omega) C(\omega) \frac{n(\omega,T)+1}{\omega} \,, \tag{14}$$

where

$$n(\omega,T) = \frac{1}{e^{\hbar\omega/kT} - 1} \tag{15}$$

is the Bose-Einstein occupation number, and $C(\omega)$ is the Raman coupling coefficient.

It has been suggested that the frequency dependence of the coupling in the SRS spectrum may follow ω^2 at very low frequencies (< 20 cm^{-1}). However, comparison between Raman and inelastic neutron scattering in inorganic glasses (GeO_2, SiO_2, B_2O_3) has shown the Raman coupling coefficient to be linear in frequency in the low terahertz range,[22–25,66,67] that is,

$$C(\omega) = \omega \tag{16}$$

and therefore, one has

$$g(\omega) \cong \frac{S^{SRS}(\omega)}{n(\omega,T)+1} \,. \tag{17}$$

The OKE spectrum is given by[61]

$$\begin{aligned} S^{OKE}(\omega) &= \chi''(\omega) \\ &= S^{SRS}(\omega) \frac{1 - e^{-\hbar\omega/kT}}{2\hbar^2} \\ &\propto g(\omega) \frac{C(\omega)}{\omega} \end{aligned} \tag{18}$$

and is also referred to as the susceptibility representation of the spontaneous depolarised Raman spectrum. Making the assumption of Eq. (16), one has

$$S^{OKE}(\omega) \cong g(\omega) \cdot \tag{19}$$

Supplementary figures

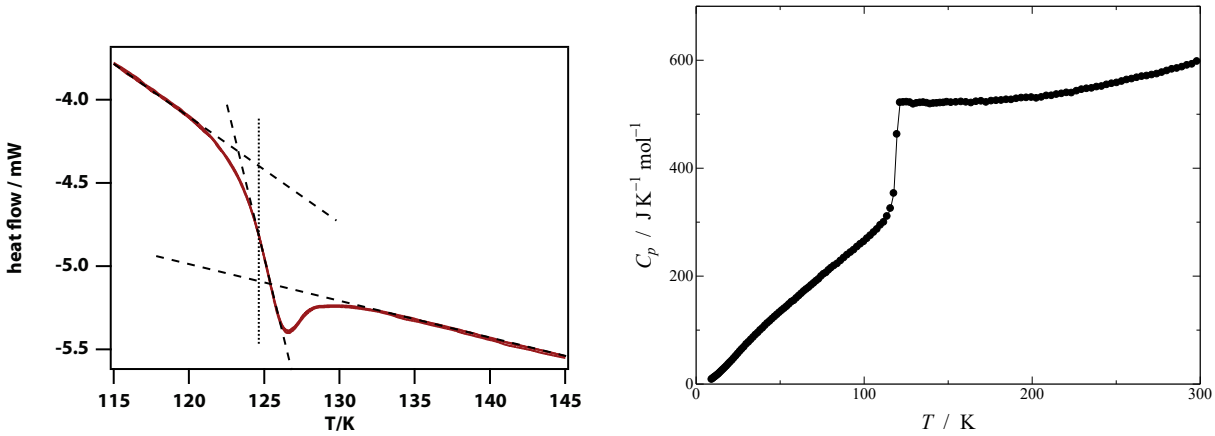

Supplementary Figure 1. Heat capacity measurements of TBOS. (**top**) Measured using the TA Instruments DSC 2500 (three scans superimposed) using quench cooling followed by controlled heating showing a glass transition at T_g = 124 K. (**bottom**) Heat capacity measured using a PPMS relaxation calorimeter (<20 K) and an adiabatic calorimeter (>10 K).

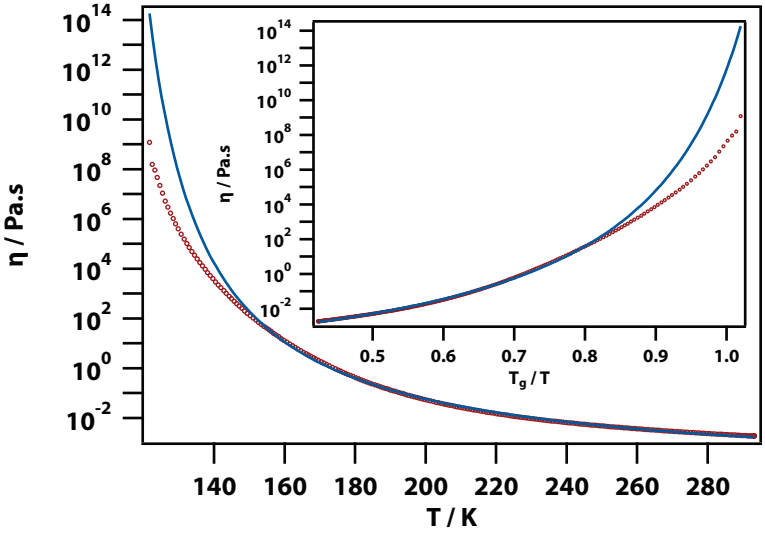

Supplementary Figure 2. Temperature dependent viscosity of TBOS and Angell plot using the measured glass transition temperature of T_g = 124 K. Also shown is a fit (using data from 150 to 293 K) to the Vogel-Fulcher-Tammann expression for viscosity, $\eta = \eta_0 \exp(DT_0/(T-T_0))$, with $\eta_0 = 4.62\ 10^{-5} \pm 0.21\ 10^{-5}$ Pa s, D = 6.4±0.1 K, and T_0 = 105.4±0.5 K.

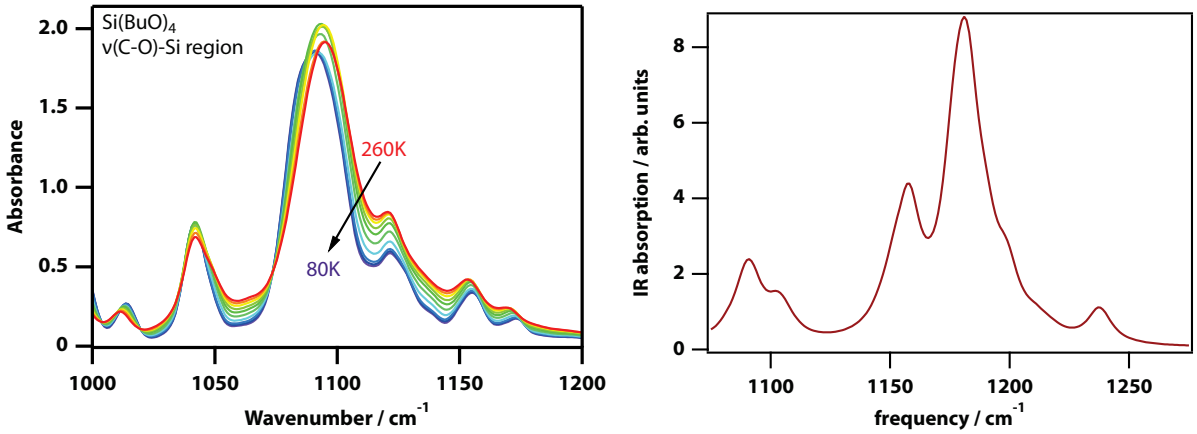

Supplementary Figure 3. Infrared spectra of TBOS in the mid-infrared region. (left) Experimental temperature-dependent IR spectra of liquid and vitrified TBOS. (right) Computed IR spectrum of TBOS.

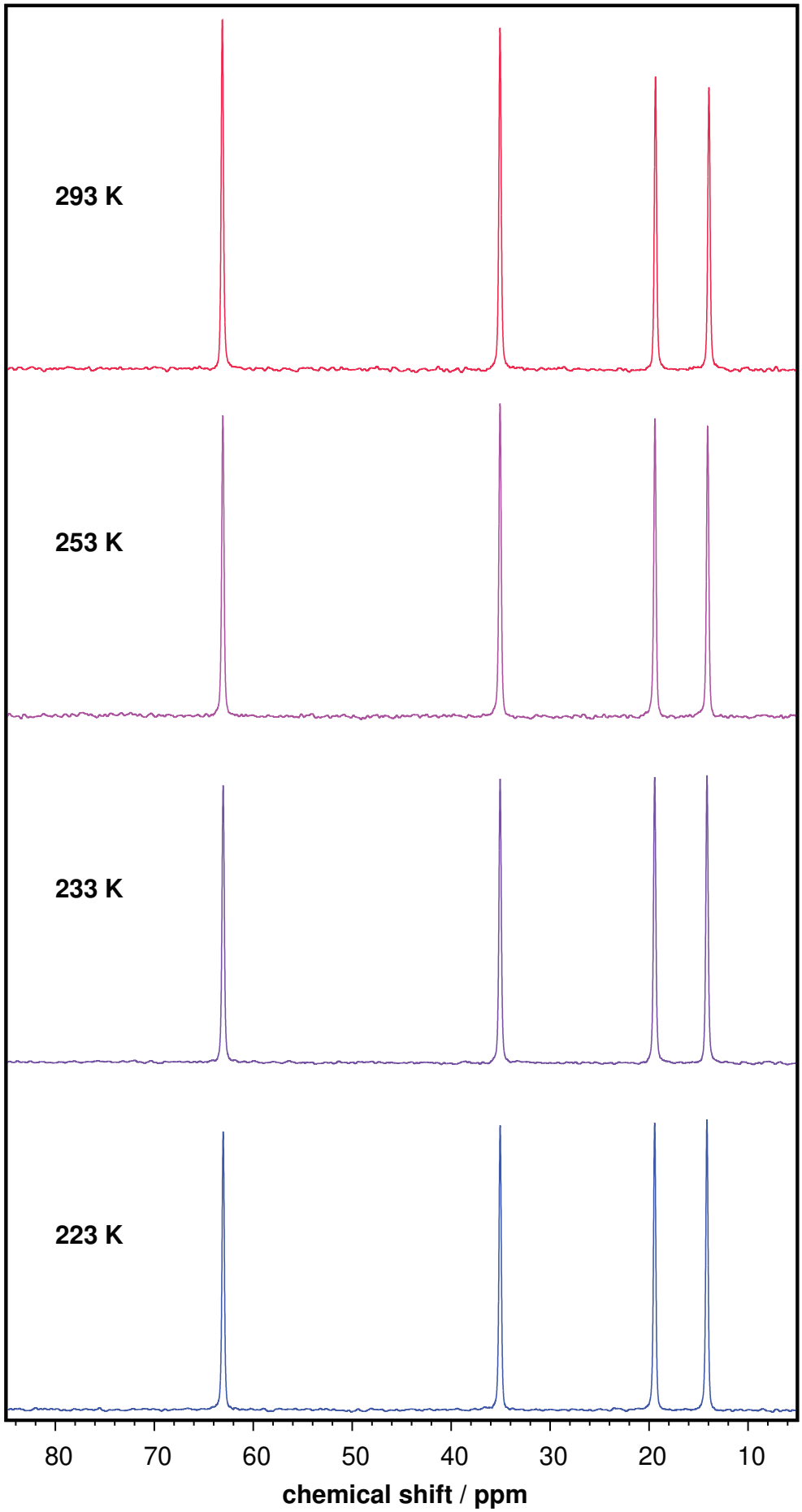

Supplementary Figure 4. Temperature-dependent ^{13}C NMR spectra of TBOS.

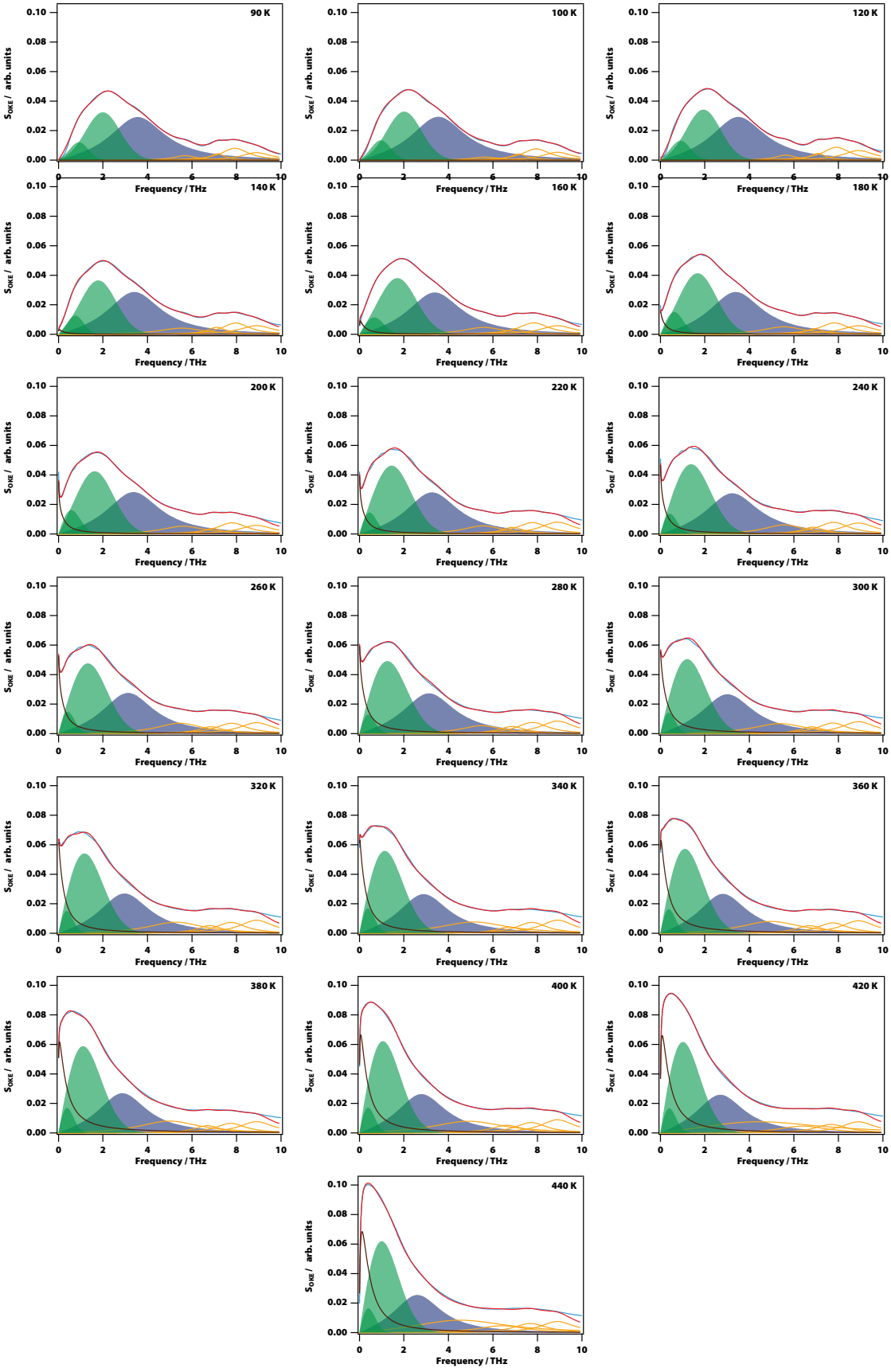

Supplementary Figure 5. All OKE data on a linear frequency scale.

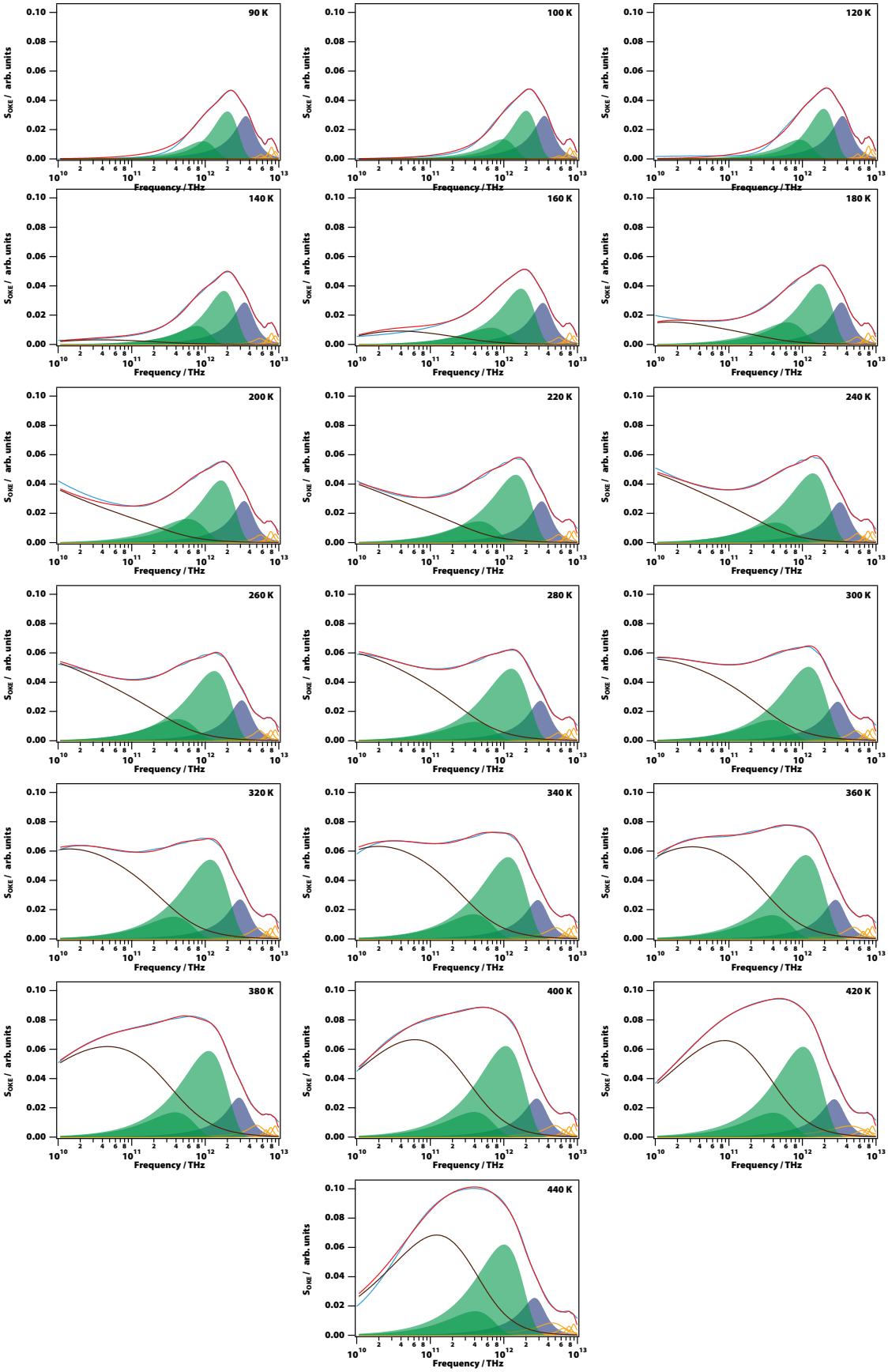

Supplementary Figure 6. All OKE data on a logarithmic frequency scale.

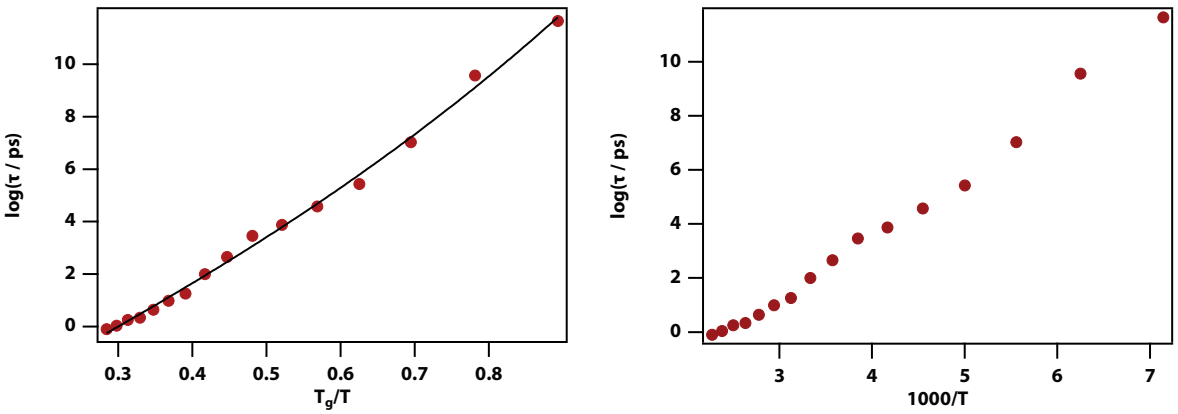

Supplementary Figure 7. Angell plot of the temperature dependent translational-relaxation time constant of TBOS using the measured glass transition temperature of T_g = 125 K. Also shown is a fit to the Stokes-Einstein expression for the translational diffusion relaxation time using a Vogel-Fulcher-Tammann expression for viscosity, $\tau = (\eta_0/T)\exp(DT_0/(T\text{-}T_0))$, with η_0 = 0.05±0.04 cP, D = 78±22 K, and T_0 = 43±8 K. (**right**) Same on a 1000/T scale.

Temp	HN				G1			G2			B1		
K	**A**	**t /ps**	**β**	**$10^{\tau rise}$ / ps**	**A**	**ω_0 / GHz**	**σ /GHz**	**A**	**ω_0 / GHz**	**σ /GHz**	**A**	**ω_0 / GHz**	**γ /GHz**
90					12727	921	420	63176	1996	776	139.6	3860	3050
100					14858	962	439	63419	2012	781	139.6	3841	3016
120					14619	908	442	66246	1938	771	139.6	3800	2996
140	19196	$4.48\ 10^{11}$	0.304	-2.00	12680	753	401	74121	1790	808	139.6	3709	2989
160	12751	$3.73\ 10^{9}$	0.304	-2.00	13978	642	429	81792	1718	855	139.6	3691	3026
180	3102	$1.07\ 10^{7}$	0.304	-1.58	16235	604	422	88345	1676	851	139.6	3687	2976
200	1689	$2.70\ 10^{5}$	0.304	9.06	19531	509	450	90485	1629	848	139.6	3676	2998
220	1192	38163	0.304	-0.88	14976	390	373	103709	1435	888	139.6	3563	2927
240	947	7550.9	0.304	-0.88	14193	356	364	107436	1359	897	139.6	3548	2988
260	868	2918.3	0.304	-0.88	15253	331	352	107429	1288	887	139.6	3431	2886
280	700	459	0.304	-0.88	13346	311	347	119019	1178	930	139.6	3435	2925
300	545	101	0.304	-0.88	14790	280	336	116984	1131	891	139.6	3331	2907
320	405	18.4	0.407	-0.88	16500	257	334	132798	1044	916	139.6	3271	2821
340	387	9.8	0.428	-0.88	17863	265	348	131696	1031	886	139.6	3197	2806
360	375	4.4	0.440	-0.88	18827	259	347	141225	954	898	139.6	3109	2714
380	373	2.2	0.448	-0.88	18994	272	348	151508	931	920	139.6	3167	2736
400	323	1.8	0.554	-0.88	20250	265	356	163610	841	904	139.6	3090	2737
420	310	1.1	0.600	-0.88	21134	258	367	164907	775	888	139.6	3000	2709
440	292	0.8	0.692	-0.88	21992	251	374	171044	734	888	139.6	2914	2673

Supplementary Table 1. ***Fit parameters used in fitting the OKE data****.HN, G_i, and B_i refers to the parameters for the Havriliak-Negami, Gaussian, and Brownian-oscillator fit functions respectively (see Supplementary note 1).*

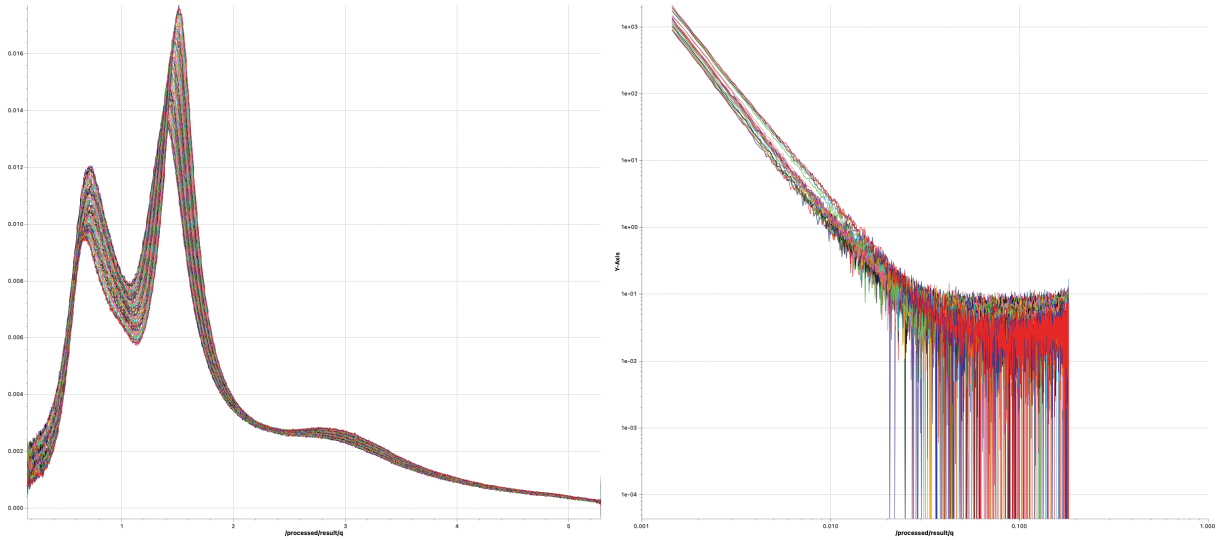

Supplementary Figure 8. Background subtracted WAXS and SAXS data on TBOS from 25° to -181°C. The SAXS data follow a Porod law with an exponent of 3.5.

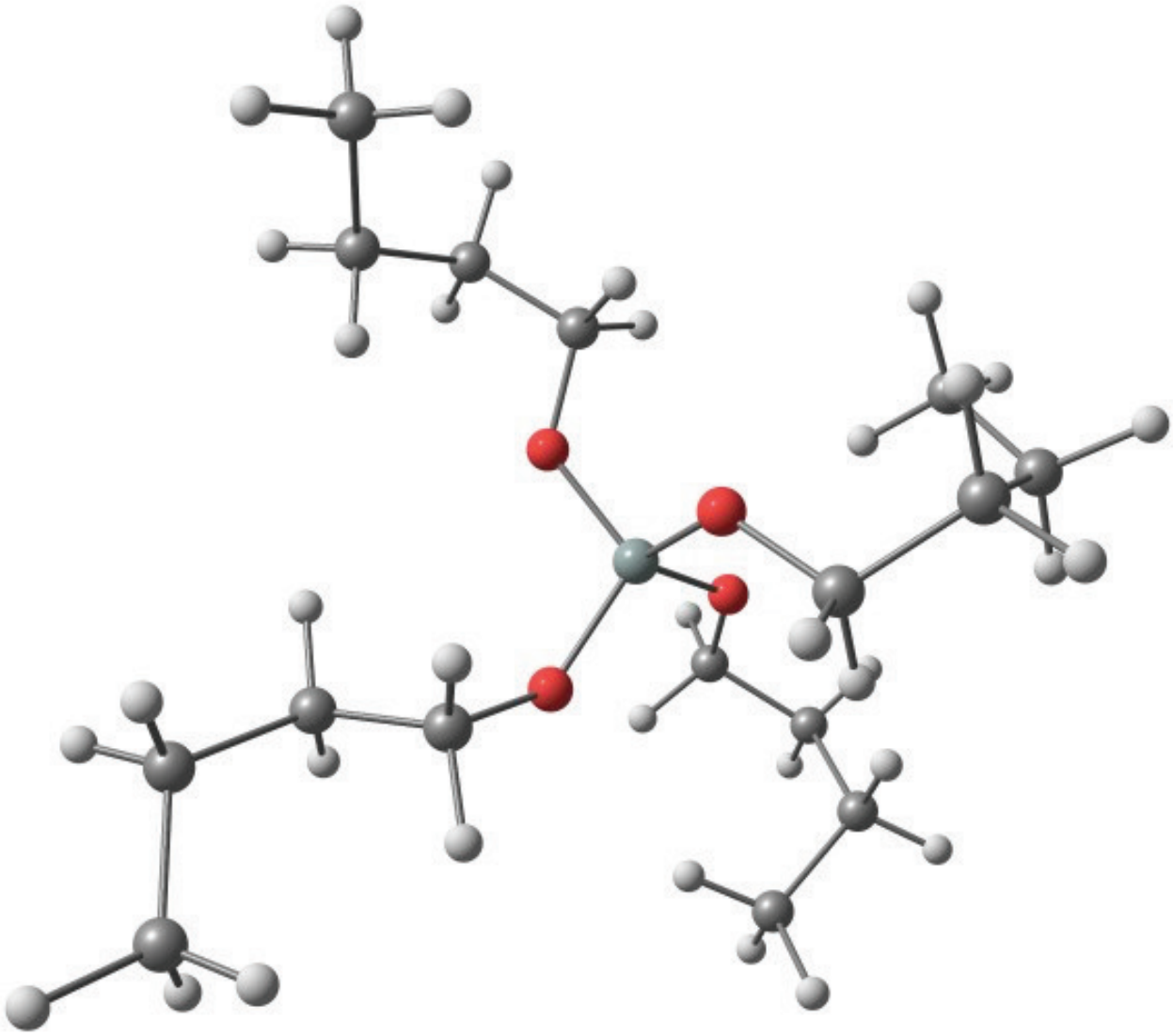

Supplementary Figure 9. Model of TBOS. Structure obtained by wB97X-D3/ma-def2-SVP. Based on the molecular weight of TBOS of 320.54 g/mol and its density at 25°C of 0.899 kg/l (Sigma-Aldrich), one calculates a molecular volume of 592 Å^3 or (assuming a spherical shape) a hydrodynamic radius of 5.2 Å.

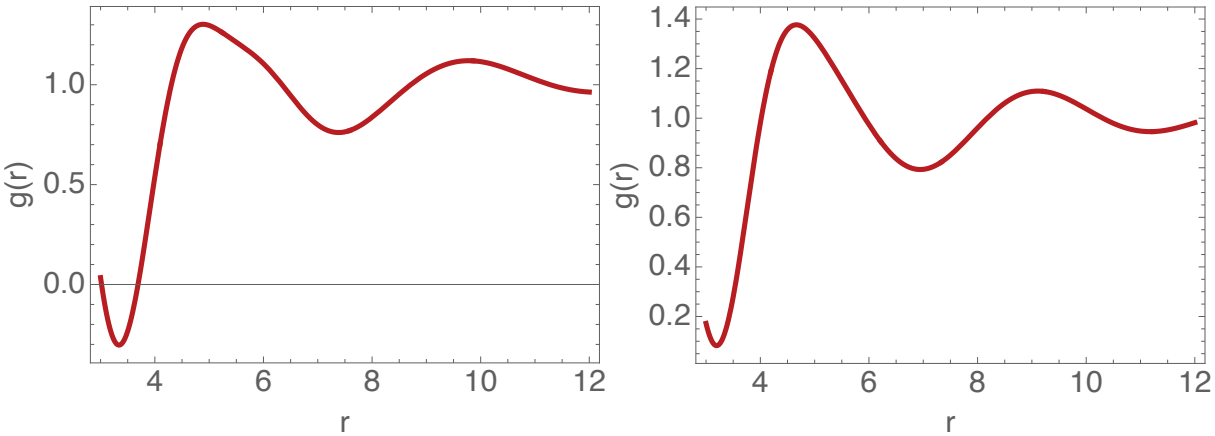

Supplementary Figure 10. Radial distribution functions calculated from the fits to the WAXS data and analytical transformation (see Supplementary note 2). Comparison of the result at 25°C (left) and -110°C (right) shows a contraction of both the first and second solvation shell.

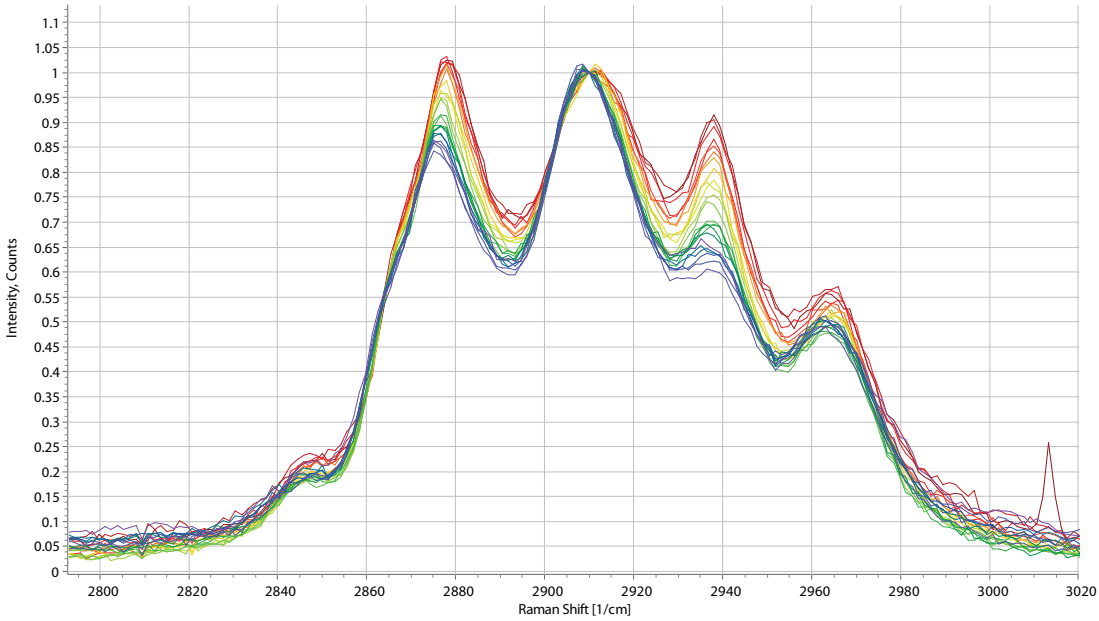

Supplementary Figure 11. Temperature dependent (40°C to -180°C) Raman spectra in the CH-stretch region of TBOS normalised at 2910 cm^{-1}. The peak height ratio I_{2885}/I_{2850} is sensitive to chain packing type,[68,69] showing that the butoxide side chains are becoming all-trans at low temperature.

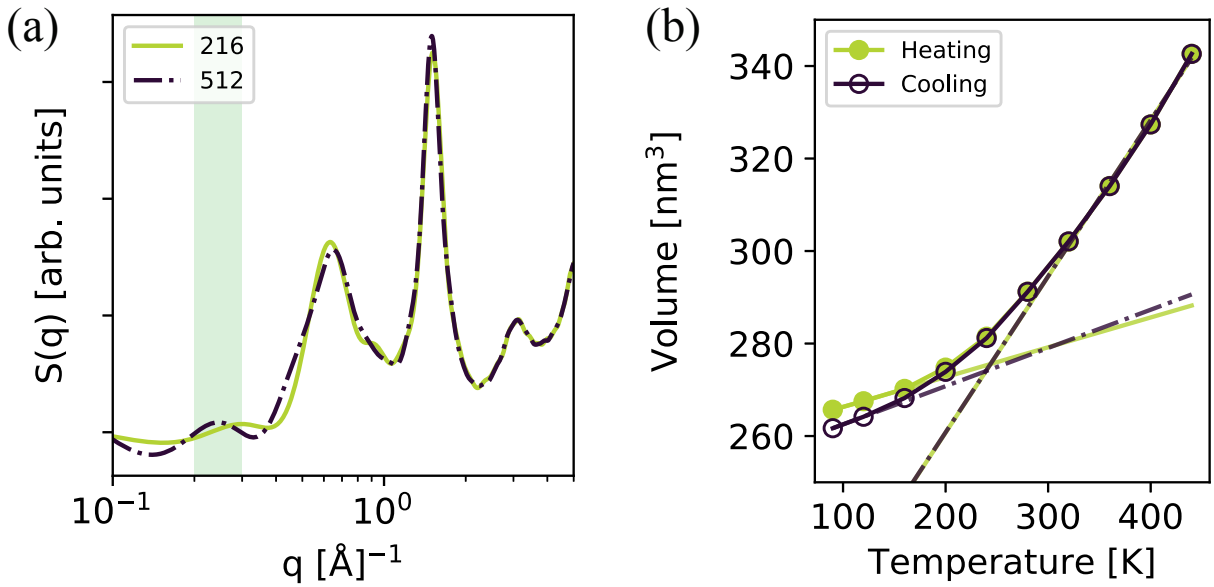

Supplementary Figure 12. Finite size effects and estimation of the glass transition temperature in the MD simulations. (a) Total (static) structure factor computed at 90K for a 216- and a 512-molecule model of TBOS. The region shaded in green highlights the emergence of the pre-peak in the structure factor discussed in the main text. (b) Average value of the simulation box for the 512-molecule model of TBOS as a function of temperature. T_g has been obtained from the intersection of the two linear fits with respect to the data points relative to the glass ($T < 200$ K) and the supercooled liquid ($T > 300$ K) respectively. The results are reported for both a heating and a cooling ramp, which give $T_g = 249 \pm 20$ and 241 ± 20 K, respectively.

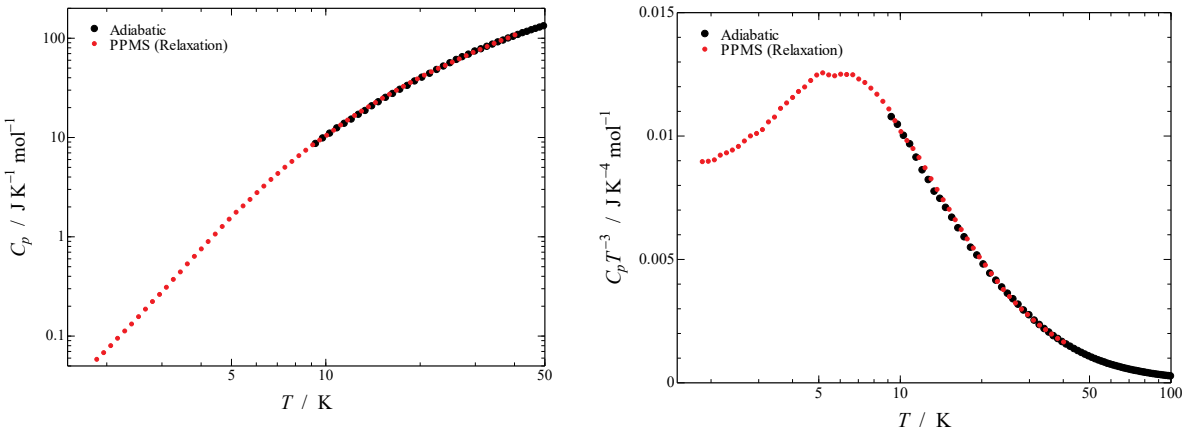

Supplementary Figure 13. Low temperature heat capacity TBOS measured using a PPMS relaxation calorimeter (<20 K) and an adiabatic calorimeter (>10 K). (left) Heat capacity and (right) heat capacity divided by temperature cubed.

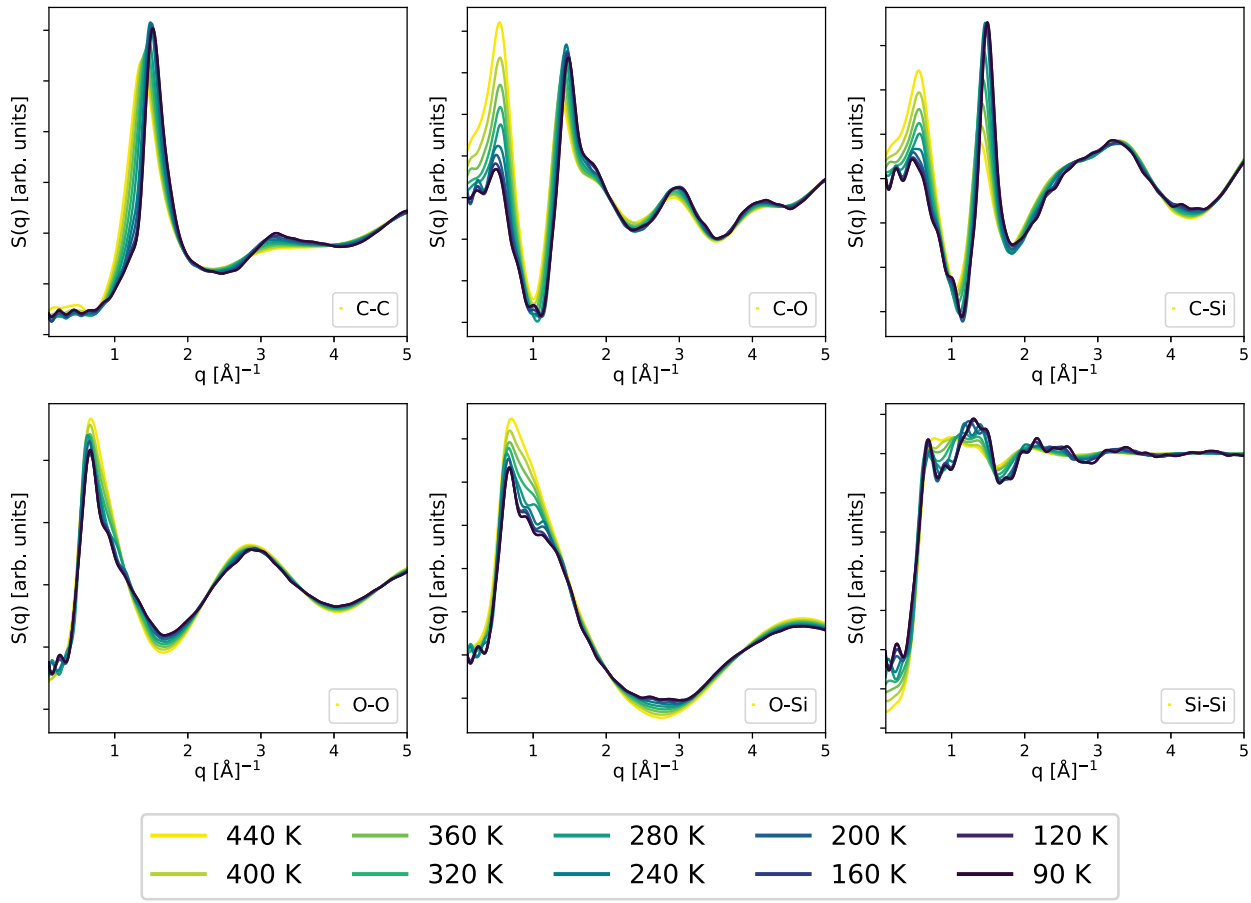

Supplementary Figure 14. (Static) structure factor for a 512-molecule model of TBOS as a function of temperature. The results are reported for every individual pair of atomic species (exception made for hydrogen atoms).

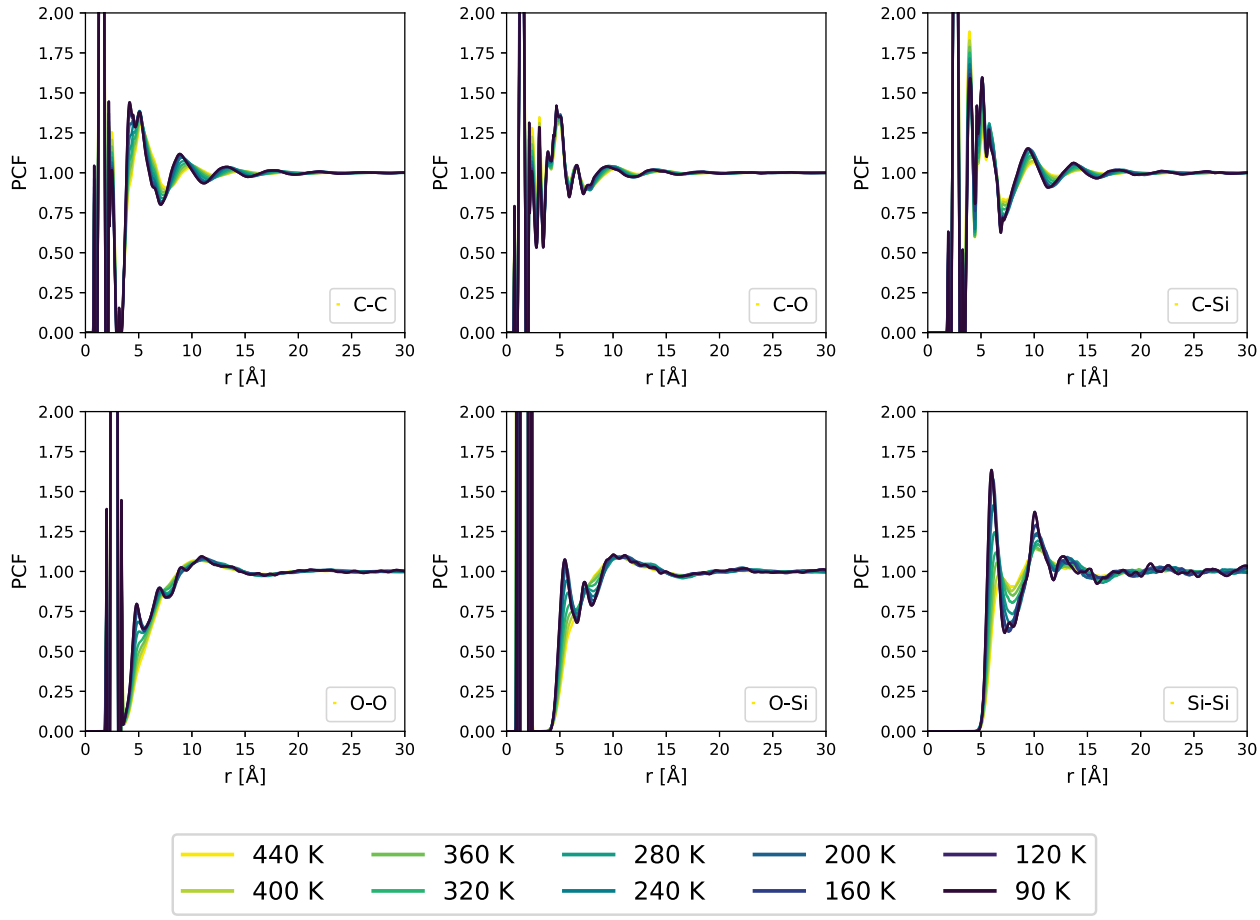

Supplementary Figure 15. Pair correlation functions (PCF) for a 512-molecule model of TBOS as a function of temperature. The results are reported for every individual pair of atomic species (exception made for hydrogen atoms).

T/°C	10^3 A_3 q_3		γ_3	10^3 A_4 q_4		γ_4	10^3 A_5 q_5		γ_5	10^3 A_6 q_6		γ_6	10^3 A_7 q_7		γ_7	10^3 A_8 q_8		γ_8
25	0.48	0.67	0.09	3.74	0.76	0.19	10.29	1.40	0.22	0.74	1.52	0.25	2.36	3.06	0.42	27.94	3.13	1.81
23	0.49	0.67	0.09	3.70	0.76	0.19	10.55	1.40	0.22	0.63	1.54	0.26	2.46	3.06	0.42	27.83	3.15	1.82
21	0.50	0.67	0.09	3.70	0.76	0.19	10.39	1.40	0.22	0.72	1.53	0.26	2.43	3.06	0.42	27.88	3.14	1.81
19	0.51	0.67	0.09	3.72	0.76	0.19	10.13	1.40	0.21	0.82	1.52	0.24	2.28	3.06	0.41	27.90	3.12	1.78
17	0.50	0.67	0.09	3.71	0.76	0.19	10.51	1.40	0.22	0.67	1.54	0.25	2.32	3.06	0.41	27.75	3.15	1.78
15	0.52	0.67	0.09	3.71	0.76	0.19	10.60	1.40	0.22	0.63	1.55	0.25	2.35	3.06	0.42	27.59	3.15	1.77
13	0.51	0.67	0.09	3.72	0.76	0.19	10.55	1.40	0.21	0.66	1.55	0.24	2.26	3.06	0.41	27.64	3.15	1.75
11	0.53	0.67	0.09	3.67	0.76	0.19	10.57	1.40	0.21	0.66	1.55	0.26	2.33	3.06	0.41	27.65	3.16	1.76
9	0.51	0.67	0.09	3.74	0.76	0.19	10.54	1.40	0.21	0.69	1.55	0.25	2.21	3.06	0.40	27.40	3.15	1.72
7	0.57	0.67	0.09	3.58	0.76	0.19	10.63	1.41	0.21	0.63	1.56	0.25	2.36	3.06	0.41	27.76	3.16	1.76
5	0.52	0.67	0.09	3.68	0.76	0.19	10.74	1.41	0.21	0.63	1.57	0.25	2.35	3.06	0.41	27.45	3.17	1.73
3	0.50	0.67	0.09	3.69	0.76	0.19	10.76	1.41	0.21	0.64	1.56	0.25	2.30	3.06	0.41	27.38	3.17	1.72
1	0.52	0.67	0.09	3.71	0.76	0.19	10.78	1.41	0.21	0.60	1.58	0.25	2.20	3.06	0.40	27.31	3.17	1.69
-1	0.51	0.67	0.09	3.69	0.76	0.19	10.79	1.41	0.21	0.62	1.58	0.25	2.26	3.06	0.41	27.36	3.17	1.70
-3	0.56	0.67	0.09	3.64	0.77	0.19	10.70	1.41	0.21	0.66	1.58	0.25	2.21	3.06	0.40	27.38	3.17	1.69
-5	0.51	0.67	0.09	3.68	0.76	0.19	10.94	1.41	0.21	0.57	1.59	0.25	2.19	3.06	0.40	27.19	3.18	1.68
-7	0.54	0.67	0.09	3.68	0.77	0.19	10.68	1.41	0.21	0.71	1.57	0.25	2.19	3.06	0.40	27.29	3.17	1.67
-9	0.56	0.67	0.09	3.70	0.77	0.20	11.00	1.42	0.21	0.58	1.61	0.25	2.22	3.06	0.40	26.91	3.19	1.65

-11	0.56	0.67	0.09	3.66	0.77	0.20	10.93	1.42	0.21	0.61	1.60	0.25	2.17	3.06	0.40	26.96	3.18	1.64
-13	0.56	0.67	0.09	3.63	0.77	0.19	10.95	1.42	0.21	0.61	1.60	0.24	2.16	3.06	0.39	27.11	3.19	1.65
-15	0.55	0.67	0.09	3.68	0.77	0.20	10.83	1.42	0.20	0.68	1.59	0.24	2.13	3.06	0.39	27.00	3.18	1.63
-17	0.56	0.67	0.09	3.64	0.77	0.20	10.97	1.42	0.20	0.60	1.61	0.24	2.14	3.06	0.39	26.99	3.18	1.63
-19	0.55	0.67	0.09	3.64	0.77	0.19	10.88	1.42	0.20	0.65	1.59	0.24	2.09	3.06	0.39	27.12	3.18	1.63
-21	0.56	0.67	0.09	3.68	0.77	0.20	10.99	1.42	0.20	0.63	1.60	0.24	2.01	3.06	0.38	26.79	3.18	1.59
-23	0.55	0.67	0.09	3.67	0.77	0.20	11.02	1.42	0.20	0.65	1.61	0.24	2.08	3.06	0.39	26.82	3.19	1.60
-25	0.56	0.67	0.09	3.70	0.77	0.20	10.98	1.42	0.20	0.66	1.60	0.24	1.95	3.05	0.38	26.73	3.18	1.57
-27	0.54	0.67	0.09	3.70	0.77	0.20	11.14	1.43	0.20	0.61	1.63	0.24	2.08	3.06	0.39	26.63	3.20	1.58
-29	0.58	0.67	0.09	3.63	0.77	0.20	11.16	1.43	0.20	0.61	1.63	0.24	2.03	3.05	0.38	26.75	3.20	1.58
-31	0.59	0.66	0.09	3.61	0.77	0.20	11.04	1.43	0.20	0.67	1.61	0.24	2.08	3.06	0.39	26.83	3.20	1.58
-33	0.57	0.67	0.09	3.66	0.77	0.20	11.17	1.43	0.20	0.63	1.63	0.24	2.04	3.05	0.38	26.60	3.20	1.56
-35	0.58	0.66	0.09	3.64	0.77	0.20	11.02	1.43	0.20	0.69	1.61	0.24	1.98	3.06	0.38	26.80	3.19	1.56
-37	0.57	0.67	0.09	3.64	0.77	0.20	11.15	1.43	0.20	0.64	1.62	0.24	1.95	3.05	0.37	26.73	3.20	1.55
-39	0.56	0.66	0.09	3.67	0.77	0.20	11.21	1.43	0.20	0.64	1.63	0.24	1.96	3.06	0.37	26.62	3.20	1.54
-41	0.55	0.67	0.09	3.69	0.77	0.20	11.18	1.43	0.20	0.66	1.63	0.24	1.92	3.05	0.37	26.55	3.20	1.53
-43	0.58	0.66	0.09	3.64	0.78	0.20	11.30	1.44	0.20	0.62	1.64	0.24	1.93	3.05	0.37	26.55	3.21	1.53
-45	0.62	0.66	0.09	3.61	0.78	0.20	11.20	1.44	0.20	0.68	1.63	0.24	1.92	3.05	0.37	26.58	3.21	1.52
-47	0.60	0.66	0.09	3.60	0.78	0.20	11.27	1.44	0.20	0.65	1.64	0.24	1.99	3.05	0.38	26.59	3.22	1.53
-49	0.61	0.66	0.09	3.62	0.78	0.20	11.32	1.44	0.20	0.69	1.65	0.25	1.99	3.05	0.38	26.40	3.22	1.51
-51	0.63	0.66	0.09	3.56	0.78	0.20	11.23	1.44	0.19	0.67	1.64	0.24	1.91	3.05	0.37	26.69	3.21	1.52
-53	0.63	0.66	0.09	3.51	0.78	0.20	11.25	1.44	0.19	0.68	1.64	0.24	2.07	3.06	0.38	26.73	3.22	1.54
-55	0.61	0.66	0.09	3.62	0.78	0.20	11.23	1.44	0.19	0.74	1.64	0.24	1.93	3.05	0.37	26.47	3.22	1.50
-57	0.63	0.66	0.09	3.59	0.78	0.20	11.33	1.44	0.19	0.69	1.65	0.24	1.90	3.05	0.37	26.47	3.22	1.49
-59	0.63	0.66	0.09	3.60	0.78	0.20	11.24	1.44	0.19	0.73	1.64	0.24	1.86	3.05	0.36	26.52	3.21	1.48
-61	0.64	0.66	0.09	3.56	0.78	0.20	11.34	1.45	0.19	0.72	1.65	0.24	1.95	3.05	0.37	26.47	3.23	1.49
-63	0.64	0.66	0.09	3.58	0.78	0.20	11.37	1.45	0.19	0.72	1.66	0.24	1.97	3.05	0.37	26.38	3.23	1.48
-65	0.65	0.66	0.09	3.56	0.78	0.20	11.49	1.45	0.19	0.69	1.67	0.25	1.94	3.05	0.37	26.35	3.24	1.48
-67	0.69	0.66	0.09	3.46	0.79	0.20	11.42	1.45	0.19	0.70	1.66	0.25	2.06	3.05	0.38	26.57	3.24	1.50
-69	0.68	0.66	0.09	3.48	0.79	0.20	11.31	1.45	0.19	0.74	1.65	0.24	1.94	3.05	0.37	26.67	3.23	1.49
-71	0.67	0.66	0.09	3.52	0.79	0.20	11.40	1.45	0.19	0.76	1.66	0.25	2.00	3.05	0.37	26.39	3.24	1.48
-73	0.67	0.66	0.09	3.55	0.79	0.20	11.36	1.45	0.19	0.79	1.65	0.24	1.89	3.05	0.36	26.38	3.23	1.46
-75	0.71	0.66	0.10	3.47	0.79	0.20	11.36	1.45	0.19	0.77	1.65	0.24	1.93	3.05	0.37	26.49	3.23	1.47
-77	0.68	0.66	0.09	3.50	0.79	0.20	11.45	1.46	0.19	0.77	1.66	0.24	1.92	3.05	0.37	26.40	3.24	1.46
-79	0.71	0.66	0.09	3.51	0.79	0.20	11.42	1.46	0.18	0.77	1.66	0.24	1.84	3.05	0.36	26.37	3.24	1.44
-81	0.72	0.66	0.09	3.45	0.79	0.20	11.33	1.46	0.18	0.80	1.65	0.24	1.87	3.05	0.36	26.58	3.23	1.46
-83	0.72	0.66	0.10	3.48	0.79	0.20	11.51	1.46	0.18	0.76	1.67	0.24	1.92	3.05	0.36	26.29	3.25	1.44
-85	0.73	0.66	0.10	3.44	0.79	0.20	11.48	1.46	0.18	0.78	1.67	0.24	1.97	3.05	0.36	26.41	3.25	1.45
-87	0.73	0.66	0.10	3.44	0.79	0.20	11.46	1.46	0.18	0.79	1.67	0.24	1.85	3.05	0.35	26.47	3.24	1.44
-89	0.71	0.66	0.09	3.50	0.79	0.20	11.59	1.46	0.18	0.79	1.68	0.25	1.90	3.04	0.36	26.15	3.25	1.42
-91	0.75	0.66	0.10	3.43	0.79	0.20	11.56	1.46	0.18	0.80	1.67	0.24	1.92	3.05	0.36	26.29	3.25	1.43
-93	0.74	0.66	0.09	3.44	0.79	0.20	11.51	1.47	0.18	0.81	1.67	0.24	1.88	3.05	0.36	26.41	3.25	1.43
-95	0.75	0.66	0.09	3.42	0.80	0.20	11.50	1.47	0.18	0.83	1.67	0.24	1.88	3.05	0.35	26.41	3.25	1.42

-97	0.77	0.66	0.10	3.39	0.80	0.20	11.52	1.47	0.18	0.82	1.67	0.24	1.92	3.05	0.36	26.48	3.26	1.43
-99	0.78	0.66	0.10	3.40	0.80	0.21	11.58	1.47	0.18	0.83	1.68	0.24	1.98	3.05	0.36	26.31	3.26	1.42
-101	0.78	0.66	0.10	3.40	0.80	0.21	11.50	1.47	0.18	0.85	1.67	0.24	1.85	3.05	0.35	26.43	3.25	1.41
-103	0.82	0.66	0.10	3.35	0.80	0.21	11.55	1.47	0.18	0.85	1.68	0.24	1.94	3.05	0.36	26.44	3.26	1.42
-105	0.84	0.65	0.10	3.29	0.80	0.21	11.61	1.47	0.18	0.83	1.69	0.24	2.04	3.05	0.36	26.49	3.27	1.43
-107	0.83	0.65	0.10	3.30	0.80	0.21	11.63	1.48	0.18	0.83	1.69	0.24	2.05	3.05	0.37	26.45	3.27	1.43
-109	0.84	0.65	0.10	3.31	0.80	0.21	11.67	1.48	0.18	0.84	1.69	0.24	2.03	3.05	0.36	26.40	3.28	1.42
-111	0.85	0.65	0.10	3.28	0.80	0.20	11.67	1.48	0.18	0.84	1.69	0.24	2.04	3.05	0.36	26.46	3.28	1.42
-113	0.85	0.65	0.10	3.28	0.80	0.21	11.66	1.48	0.18	0.83	1.69	0.24	2.04	3.05	0.36	26.49	3.28	1.42
-115	0.85	0.65	0.10	3.27	0.80	0.21	11.84	1.48	0.18	0.84	1.71	0.25	2.21	3.05	0.37	26.31	3.30	1.43
-117	0.86	0.65	0.10	3.25	0.81	0.21	11.68	1.48	0.17	0.85	1.68	0.24	2.02	3.05	0.36	26.55	3.28	1.42
-119	0.86	0.65	0.10	3.30	0.80	0.21	11.80	1.48	0.17	0.86	1.70	0.24	2.07	3.05	0.36	26.30	3.29	1.40
-121	0.87	0.65	0.10	3.26	0.81	0.21	11.84	1.49	0.17	0.85	1.70	0.24	2.11	3.05	0.36	26.31	3.30	1.40
-123	0.89	0.65	0.10	3.21	0.81	0.21	11.85	1.49	0.17	0.85	1.71	0.25	2.19	3.05	0.37	26.41	3.30	1.42
-125	0.85	0.65	0.10	3.32	0.81	0.21	11.83	1.49	0.17	0.89	1.70	0.25	2.06	3.05	0.36	26.26	3.30	1.39
-127	0.89	0.65	0.10	3.21	0.81	0.21	11.82	1.49	0.17	0.86	1.70	0.24	2.11	3.05	0.36	26.50	3.30	1.41
-129	0.90	0.65	0.10	3.19	0.81	0.21	11.93	1.49	0.17	0.84	1.71	0.24	2.13	3.05	0.36	26.40	3.30	1.40
-131	0.94	0.65	0.10	3.16	0.81	0.21	11.84	1.49	0.17	0.88	1.70	0.24	2.16	3.06	0.36	26.43	3.30	1.40
-133	0.93	0.65	0.10	3.17	0.81	0.21	11.87	1.49	0.17	0.89	1.71	0.24	2.16	3.05	0.36	26.37	3.30	1.40
-135	0.93	0.65	0.10	3.20	0.81	0.21	11.95	1.50	0.17	0.91	1.72	0.25	2.24	3.05	0.36	26.21	3.32	1.40
-137	0.94	0.65	0.10	3.19	0.81	0.21	11.97	1.50	0.17	0.89	1.71	0.24	2.19	3.05	0.36	26.18	3.31	1.39
-139	0.98	0.65	0.10	3.11	0.82	0.21	11.98	1.50	0.17	0.88	1.72	0.25	2.24	3.05	0.36	26.29	3.31	1.40
-141	1.02	0.64	0.10	3.02	0.82	0.21	11.96	1.50	0.17	0.85	1.71	0.24	2.25	3.06	0.36	26.52	3.31	1.41
-143	0.99	0.64	0.10	3.12	0.82	0.21	12.11	1.50	0.17	0.89	1.73	0.25	2.30	3.05	0.36	26.12	3.33	1.39
-145	0.98	0.64	0.10	3.15	0.81	0.21	12.25	1.50	0.17	0.92	1.75	0.26	2.54	3.05	0.38	25.88	3.35	1.40
-147	1.02	0.64	0.10	3.04	0.82	0.21	12.06	1.51	0.17	0.90	1.72	0.25	2.36	3.05	0.37	26.30	3.33	1.40
-149	0.95	0.64	0.10	3.26	0.81	0.21	12.37	1.51	0.17	1.09	1.76	0.28	2.84	3.04	0.40	25.22	3.40	1.39
-151	1.01	0.64	0.10	3.10	0.82	0.21	12.19	1.51	0.17	0.92	1.74	0.25	2.41	3.05	0.37	26.05	3.34	1.39
-153	0.99	0.64	0.10	3.13	0.82	0.21	12.30	1.51	0.17	0.96	1.75	0.26	2.60	3.05	0.38	25.77	3.37	1.39
-155	1.01	0.64	0.10	3.10	0.82	0.21	12.28	1.51	0.17	0.93	1.74	0.26	2.51	3.05	0.37	25.88	3.36	1.38
-157	1.00	0.64	0.10	3.15	0.81	0.21	12.47	1.51	0.17	1.02	1.77	0.28	2.86	3.04	0.39	25.38	3.40	1.39
-159	0.99	0.64	0.10	3.22	0.81	0.22	12.59	1.51	0.17	1.13	1.79	0.29	3.18	3.04	0.41	24.87	3.44	1.39
-161	1.05	0.64	0.10	3.08	0.82	0.21	12.47	1.52	0.17	1.07	1.78	0.28	3.04	3.04	0.40	25.33	3.42	1.41
-163	1.04	0.64	0.10	3.10	0.82	0.21	12.49	1.52	0.17	1.03	1.77	0.28	2.86	3.05	0.39	25.27	3.40	1.38
-165	1.01	0.64	0.10	3.15	0.82	0.22	12.60	1.52	0.17	1.07	1.79	-0.28	3.04	3.04	0.40	25.03	3.43	1.38
-167	1.03	0.64	0.10	3.10	0.82	0.21	12.46	1.52	0.17	1.03	1.77	-0.28	2.73	3.05	0.38	25.34	3.39	1.37
-169	1.03	0.64	0.10	3.10	0.82	0.21	12.56	1.52	0.17	1.05	1.78	-0.28	2.96	3.05	0.39	25.18	3.42	1.38
-171	1.01	0.64	0.10	3.14	0.82	0.21	12.58	1.52	0.17	1.08	1.78	-0.28	2.96	3.04	0.39	25.04	3.42	1.37
-173	1.02	0.64	0.10	3.10	0.82	0.21	12.59	1.52	0.17	1.05	1.79	-0.28	2.93	3.05	0.39	25.22	3.42	1.38
-175	1.05	0.64	0.10	3.03	0.82	0.21	12.58	1.52	0.17	1.00	1.78	-0.27	2.87	3.05	0.39	25.37	3.40	1.38
-177	1.05	0.64	0.10	3.00	0.82	0.21	12.48	1.52	0.17	0.95	1.76	-0.27	2.64	3.06	0.37	25.67	3.38	1.38
-179	1.01	0.64	0.10	3.09	0.82	0.21	12.57	1.52	0.17	1.03	1.78	-0.27	2.93	3.05	0.39	25.29	3.41	1.38

Supplementary Table 2. *Fit parameters temperature dependent WAXS data.*

10^3 A_1	38.40	10^3 A_2	0.020	10^3 A_3	1.368	10^3 A_4	0.521	10^3 A_5	6.435	10^3 A_6	0.477	10^3 A_7	2.550	10^3 A_8	9.947
N	3.62	q_2	0.234	q_3	0.681	q_4	0.988	q_5	1.521	q_6	1.927	q_7	3.022	q_8	3.787
		γ_2	0.063	γ_3	0.144	γ_4	0.128	γ_5	0.181	γ_6	0.263	γ_7	0.498	γ_8	1.445

Supplementary Table 3. *Fit parameters WAXS data averaged for temperature ≤ 110 K.*